

# Kinetic Inductance of Few-Layer NbSe<sub>2</sub> in the Two-Dimensional Limit

Sameia Zaman<sup>1,2</sup>, Joel I.-j. Wang<sup>1\*</sup>, Thomas Werkmeister<sup>3</sup>, Miuko Tanaka<sup>1</sup>, Thao Dinh<sup>4</sup>, Max Hays<sup>1</sup>, Daniel Rodan-Legrain<sup>1</sup>, Aranya Goswami<sup>1</sup>, Réouven Assouly<sup>1</sup>, Ahmet Kemal Demir<sup>4</sup>, David K. Kim<sup>5</sup>, Bethany M. Niedzielski<sup>5</sup>, Kyle Serniak<sup>1,5</sup>, Mollie E. Schwartz<sup>5</sup>, Kenji Watanabe<sup>6</sup>, Takashi Taniguchi<sup>7</sup>, Philip Kim<sup>3,8</sup>, Riccardo Comin<sup>4</sup>, Jeffrey A. Grover<sup>1</sup>, Terry P. Orlando<sup>1,2</sup>, Pablo Jarillo-Herrero<sup>4</sup>, and William D. Oliver<sup>1,2,4\*</sup>

<sup>1</sup>Research Laboratory of Electronics, Massachusetts Institute of Technology, Cambridge, MA 02139, USA

<sup>2</sup>Department of Electrical Engineering and Computer Science, Massachusetts Institute of Technology, Cambridge, MA 02139, USA

<sup>3</sup>John A. Paulson School of Engineering and Applied Sciences, Harvard University, Cambridge, MA, USA

<sup>4</sup>Department of Physics, Massachusetts Institute of Technology, Cambridge, MA 02139, USA

<sup>5</sup>Lincoln Laboratory, Massachusetts Institute of Technology, Lexington, MA 02421, USA

<sup>6</sup>Research Center for Electronic and Optical Materials, National Institute for Materials Science, 1-1 Namiki, Tsukuba 305-0044, Japan

<sup>7</sup>Research Center for Materials Nanoarchitectonics, National Institute for Materials Science, 1-1 Namiki, Tsukuba 305-0044, Japan

<sup>8</sup>Department of Physics, Harvard University, Cambridge, MA, USA

\*To whom correspondence should be addressed: [joelwang@mit.edu](mailto:joelwang@mit.edu), and [william.oliver@mit.edu](mailto:william.oliver@mit.edu)

## Abstract

Van der Waals (vdW) superconductors remain superconducting down to the monolayer limit, enabling the exploration of emergent physical phenomena and functionality driven by reduced dimensionality. Here, we report the characterization of the kinetic inductance of atomically thin NbSe<sub>2</sub>, a two-dimensional van der Waals superconductor, using superconducting coplanar waveguides and microwave measurement techniques familiar to circuit quantum electrodynamics (cQED). The kinetic inductance scales inversely with the number of NbSe<sub>2</sub> layers, reaching 1.2 nH/□ in the monolayer limit. Furthermore, the measured kinetic inductance exhibits a thickness-dependent crossover from clean- to dirty-limit behavior, with enhanced dirty-limit contributions emerging in the ultra-thin regime. These effects are likely driven by increased surface scattering, multi-band superconductivity, and geometric confinement. Additionally, the self-Kerr nonlinearity of the NbSe<sub>2</sub> films ranges from  $K/2\pi = -0.008$  to  $-14.7$  Hz/photon, indicating its strong potential in applications requiring compact, nearly linear, high-inductance superconducting quantum devices and detectors. The fabrication and characterization techniques demonstrated here are extensible to the investigation of other two-dimensional superconductors.

## Introduction

Kinetic inductance ( $L_k$ ) in a superconductor arises from the inertia of Cooper pair transport in response to a varying electromagnetic field. Unlike geometric inductance, which varies with the geometry of the electronic element, kinetic inductance depends on intrinsic properties of the material, e.g., superfluid density, carrier effective mass, and film thickness. For example, in a clean superconductor, the kinetic inductance per square is  $L_{k,\text{sq}} = m_{\text{eff}}/e^2 n_0 d$ , where  $m_{\text{eff}}$  is the effective mass of the charge carriers,  $n_0$  is the superfluid density (number of Cooper pairs per unit volume) per unit thickness, and  $d$  is the thickness of the sample. This relation indicates that  $L_{k,\text{sq}}$  increases with decreasing film thickness or suppressed superfluid density. Such an enhancement is useful in quantum circuits, where superconductors with high- $L_k$  are used to realize superinductors — inductive elements with a reactance that approaches and even exceeds the quantum unit  $R_Q = h/(2e)^2 = 6.4$  kΩ for Cooper pairs, where  $h$  is the Planck constant, and  $e$  is the elementary charge. Furthermore, the kinetic inductance in a superconductor is directly related to the superfluid stiffness; probing it enables insight into several fundamental properties such as the superconducting gap structure and pairing symmetry in unconventional superconductors [1–6].

Superconductors are used in a variety of applications, including in superconducting qubit circuits such as fluxonium and  $0-\pi$  qubits, which require large (and ideally linear) shunt inductance [7, 8]. They have also been used to realize coherent quantum phase slip circuits [9, 10], long-range coupling for spin qubits [11], and tailored Kerr non-linearities in light-matter interactions [12, 13]. Furthermore, these materials can be used for wide-band parametric amplifiers and high-impedance readout resonators [14–18]. For many of these applications, low- $L_k$  aluminum is used, and thus, large inductance is realized primarily by an array of Al-AlO<sub>x</sub>-Al Josephson junctions [19–21]. However, these junctions exhibit strong nonlinearity and are therefore limited in the current they can support while remaining in the linear inductance regime. This motivates the search for alternative materials that can provide large inductance with minimal nonlinearity. Recent efforts toward this goal have focused on implementing superconductors using amorphous superconducting thin films, such as TiN [22, 23], NbN [24, 25], NbTiN [26, 27], InO<sub>x</sub> [9, 28], NbSi [29], WSi [30], AlO<sub>x</sub> [31], and granular Al [32, 33]. The inherent disorder of these materials suppresses the density of Cooper-pairs, leading to high- $L_k$  in the superconducting regime [34]. Typically, these amorphous superconductors operate in the dirty limit, where the mean free path of charge carriers is shorter than the superconducting coherence length [35]. This relationship implies that, in the BCS framework, the size of a Cooper pair is greater than the average travel distance between consecutive scattering sites. In contrast, the coherence length of a clean superconductor is shorter than its mean free path, and Cooper pair transport can be regarded as ballistic when the length of the device is shorter than the mean free path.

In superconducting quantum devices, disorder and the resulting scattering of charge carriers are expected to affect quasiparticle dynamics and, consequently, device coherence. While the link between disorder, quasiparticle generation, and the associated noise remains an area of active investigation [32, 36–38], microwave characterization of superconductors with varied disorder levels may offer a way to probe their dynamic responses and help explore the role of scattering in decoherence [38].

## NbSe<sub>2</sub>—a van der Waals Superconductor

We investigate 2H-NbSe<sub>2</sub> (further referred to as NbSe<sub>2</sub> for brevity), a transition-metal dichalcogenide and a type-II superconductor. The lattice structure of NbSe<sub>2</sub> is hexagonal, with the Nb atoms in trigonal prismatic coordination surrounded by Se atoms (Fig. 1a). The layers are stacked in an ABAB sequence along the c-axis and are bonded by van der Waals forces between adjacent layers. NbSe<sub>2</sub> possesses out-of-plane mirror symmetry and broken in-plane inversion symmetry. This broken in-plane symmetry gives rise to an unconventional Ising spin-orbit coupling, which maintains superconductivity in the presence of a strong in-plane magnetic field exceeding 30 T, as observed in the monolayer limit [39, 40]. Both superconductivity

and the charge-density wave transition exist from the bulk down to monolayer thickness. However, the superconducting transition temperature ( $T_c$ ) decreases with reduced film thickness, attributable to a suppressed Cooper-pair density, the presence of a superconductor–vacuum interface, and modifications to the electronic band structure [41, 42]. As the thickness is reduced,  $\text{NbSe}_2$  exhibits several unusual quantum phenomena—including thickness-dependent Higgs modes [43], dissipationless phase diagrams [44], unconventional finite momentum pairing [45–47], and the emergence of a quantum metallic phase under a small perpendicular magnetic field [48]. Prior direct current (DC) transport studies indicate that the carrier mean free path in  $\text{NbSe}_2$  decreases with its thickness due to enhanced surface scattering [41, 44]. When encapsulated by hBN, even bilayer and monolayer  $\text{NbSe}_2$  exhibit mean free paths (approximately 17 nm and 15 nm, respectively) that are larger than their corresponding superconducting coherence length (8 nm) [40, 41, 45]. These DC transport measurements are consistent with encapsulated  $\text{NbSe}_2$  exhibiting superconductivity in the clean limit [41, 49–51].

While previous studies have primarily relied on DC transport to probe only the real part of the conductivity, in this work, we measure the kinetic inductance to access the complex conductivity of few-layer  $\text{NbSe}_2$  in the two-dimensional limit. This method allows us to determine whether the material lies in the clean limit, the dirty limit, or an intermediate regime. Moreover, it is sensitive to fundamental superconducting properties such as superfluid stiffness, surface impedance, and loss mechanisms [4, 52, 53], providing insight into the material suitability for superconducting quantum devices operating in the microwave regime.

## Device Design

We study the kinetic inductance of hBN-encapsulated  $\text{NbSe}_2$  thin films using quarter-wavelength  $\lambda/4$  coplanar waveguide (CPW) resonators made of thin-film Al. The resonant frequency of a resonator is  $f_r = \frac{1}{2\pi\sqrt{L_{\text{eff}}C_{\text{eff}}}}$ , where  $L_{\text{eff}}$  and  $C_{\text{eff}}$  are the effective inductance and capacitance of the resonator, respectively (Fig. 1b, left panel). The Al inductance is primarily geometric, and its kinetic inductance per square is much smaller than that of  $\text{NbSe}_2$ . When the  $\lambda/4$ -resonator is terminated to ground by an  $\text{NbSe}_2$  sample, the resonant frequency shifts to a lower frequency  $f_{r'} = \frac{1}{2\pi\sqrt{L'_{\text{eff}}C'_{\text{eff}}}}$  due to the additional kinetic inductance from the  $\text{NbSe}_2$  (Fig. 1b, right panel). We perform microwave simulations to determine the expected frequency shift of a  $\lambda/4$ -resonator due to the additional inductance  $L_k$  (Fig. 1c). The Al-only resonator has a frequency of 5.6 GHz. When terminated by  $\text{NbSe}_2$ , the resonance frequency decreases by 200 MHz per 0.1 nH of added termination inductance.

Figure 2a shows an optical micrograph of the superconducting circuit with  $\lambda/4$  CPW resonators used for

this work. The aluminum CPW resonators are fabricated from a 250 nm Al film deposited on a high-resistivity silicon substrate and patterned using a combination of photolithography and wet etching (see Ref. [4] and Supplementary Information for details). Two  $\lambda/4$ -resonators, an aluminum *spectator* resonator and an *experiment* resonator, are capacitively coupled to a common feedline. The spectator resonator is used as a witness to monitor the impact of the vdW materials fabrication process (without incorporating vdW materials), while the experiment resonator is terminated by a  $\text{NbSe}_2$  sample situated within a square hosting window of size 200  $\mu\text{m}$  by 200  $\mu\text{m}$ . To extract the kinetic inductance of each  $\text{NbSe}_2$  device, we analyze two  $\lambda/4$ -resonators: the  $\text{NbSe}_2$ -terminated experiment resonator (Fig. 2b) and a control resonator of the same geometry that is terminated instead by a 250 nm-thick aluminum film (Fig. 2c). The  $\text{NbSe}_2$  thin film is encapsulated in hBN to maintain a nominally clean and atomically flat interface while ensuring a relatively low-microwave-loss environment [53, 54]. This hBN- $\text{NbSe}_2$ -hBN heterostructure is assembled through mechanical exfoliation and standard dry-transfer techniques inside an argon-filled glove box, ensuring minimal oxidation of the  $\text{NbSe}_2$  before full encapsulation.

The hBN- $\text{NbSe}_2$ -hBN heterostructure is galvanically connected to the microwave resonator and the ground plane. To achieve a highly transparent, superconducting contact, we make a one-dimensional edge-contact to the  $\text{NbSe}_2$  using reactive ion etching of the heterostructure, followed by in-situ argon ion milling and aluminum deposition (Fig. 2d) [55]. A low-loss superconducting contact is critical to maintaining a narrow resonance line (i.e., a high quality factor of the resonator), which translates to higher measurement resolution of the resonator frequency. Details of the fabrication process and the verification of the superconducting contact are provided in the Supplementary Information.

## Microwave Characterization of $\text{NbSe}_2$

The samples are characterized in a dilution refrigerator with a base temperature of approximately 10 mK (see Fig. S2 for wiring diagram). The microwave transmission coefficient  $S_{21}$  is measured as a function of frequency using a two-port vector network analyzer (VNA). Figure 3a shows a representative  $|S_{21}|$  measurement from a  $\lambda/4$ -resonator terminated by a 9-nm-thick (determined by AFM)  $\text{NbSe}_2$  film (Device ID D6). The resonant frequency  $f_{\text{r},\text{Al}-\text{NbSe}_2}$  and quality factor are determined from a Lorentzian fit using the standard circular fit procedure [56] (Fig. 3a inset and Supplementary Information). In the single-photon limit, the  $\text{NbSe}_2$ -terminated resonator exhibits a resonant frequency  $f_{\text{r},\text{Al}-\text{NbSe}_2} = 4.79 \text{ GHz}$  and an internal quality factor  $Q_{\text{i},\text{Al}-\text{NbSe}_2} = 2.8 \times 10^4$ , while the Al-terminated control resonator has a resonant frequency  $f_{\text{r},\text{Al}} = 5.34 \text{ GHz}$  and an internal quality factor  $Q_{\text{i},\text{Al}} = 1.0 \times 10^5$ . The lower internal quality factor observed in the  $\text{NbSe}_2$ -terminated Al resonator is likely due to additional dissipation arising from imperfect electrical contacts

between the Al and the  $\text{NbSe}_2$ , as well as dielectric loss introduced by residual polymer contamination from the dry transfer process. Moreover, the frequency difference  $f_{\text{r,Al}} - f_{\text{r,Al-NbSe}_2} = 0.45 \text{ GHz}$  highlights the impact of terminating the resonator with  $\text{NbSe}_2$  and enables us to extract a kinetic inductance  $L_{\text{k,sq}} = 124 \text{ pH}$  for this  $\text{NbSe}_2$  sample.

The resonant frequency of the  $\text{NbSe}_2$ -terminated resonator decreases with increasing microwave probe power, e.g., with a noticeable downshift in  $f_{\text{r,Al-NbSe}_2}$  at the estimated sample power of  $-90 \text{ dBm}$  (Fig. 3b, green arrow). This frequency downshift indicates a contribution from kinetic inductance. As the microwave power increases, enhanced Cooper-pair breaking leads to a reduction in the superfluid density ( $n_0$ ), resulting in a larger kinetic inductance  $L_{\text{k}}$  and, consequently, a lower resonant frequency. In contrast, the aluminum resonator exhibits no observable power dependence up to an estimated input power of  $-60 \text{ dBm}$  at the sample (Fig. S4b), corresponding to the upper limit of our VNA output (VNA outputs a power of  $10 \text{ dBm}$  at room temperature, which is reduced to  $-60 \text{ dBm}$  at the sample after passing through a total attenuation of  $70 \text{ dB}$ ), confirming that its inductance is predominantly geometric. The nonlinear microwave power dependence exhibited by the  $\text{NbSe}_2$ -terminated resonator, observed over the power range from  $-100 \text{ dBm}$  to  $-80 \text{ dBm}$ , is well-described by a Kerr-type or Duffing-type nonlinearity [57] (see Supplementary Information). When the microwave power in the resonator exceeds a critical threshold, the resonant frequency bifurcates and enters a bistability regime (Fig. 3b, blue arrow) [58–60]. From a linear fit of the resonant frequency shift ( $\Delta f = f_{\text{r,Al-NbSe}_2}(n_{\text{r}} = 1) - f_{\text{r,Al-NbSe}_2}(n_{\text{r}})$ ) with the photon number of the resonator ( $n_{\text{r}}$ ), shown in Fig. 3c, we extract a self-Kerr coefficient  $K/2\pi = -1.7 \text{ Hz/photon}$  at  $10 \text{ mK}$ . Typically, conventional superconducting inductors of similar dimensions, such as granular aluminum, with a self-Kerr coefficient of  $4.5 \text{ MHz}$  [61], and Josephson junction arrays, with a self-Kerr of  $8 \text{ MHz}$  [62]—exhibit significantly higher nonlinearity. In contrast,  $\text{NbSe}_2$  films show a lower self-Kerr coefficient, indicating low nonlinearity.

We also investigate the dependence of the kinetic inductance on the DC bias current. A DC bias current  $I_{\text{DC}}$  is introduced via a contact to the microwave line just above the  $\text{NbSe}_2$  termination (Fig. 3d), while a microwave tone is maintained in the low-power linear regime ( $P_{\text{rf}} = -120 \text{ dBm}$ ). The resonant frequency ( $f_{\text{r,Al-NbSe}_2}$ ) decreases with an increasing bias current (up to  $I_{\text{DC}} = 30 \mu\text{A}$ ), indicating a corresponding increase in kinetic inductance (Fig. 3e). This behavior is similar to the microwave response due to the Kerr-type nonlinearity. In the Ginzburg-Landau framework, the dependence of kinetic inductance of the superconducting film with bias current is well-described by a quadratic function (ignoring the terms beyond

2<sup>nd</sup> order) [35]:

$$L_k(I_{\text{DC}}) = L_k(0) \left[ 1 + \left( \frac{I_{\text{DC}}}{I^*} \right)^2 + \dots \right], \quad (1)$$

where  $L_k(0)$  is the kinetic inductance of the resonator at zero current bias, and  $I^*$  is a characteristic current, also known as the depairing current.  $I^*$  is typically comparable to the superconducting critical current  $I_c$ , and sets the scale of non-linearity. By fitting to this relationship,  $I^*$  is determined to be 0.4 mA for the 9 nm thick, 3.9  $\mu\text{m}$  wide NbSe<sub>2</sub> sample. We observe that both the resonant frequency and the kinetic inductance per square exhibit a quadratic dependence on the DC bias current (Fig. 3f), consistent with the anisotropic nodeless pairing of NbSe<sub>2</sub> reported in previous studies [46, 63].

### Layer Dependence of $L_k$ in NbSe<sub>2</sub>

VdW superconductors remain superconducting in the monolayer limit [39, 64], which enables one to increase kinetic inductance by reducing the thickness. Figure 4a shows the sheet kinetic inductance ( $L_{k,\text{sq}}$ ) of NbSe<sub>2</sub> films extracted from microwave measurements as a function of thickness ( $d$ ) and the corresponding layer numbers. The measured  $L_{k,\text{sq}}$  (red circles) exhibits an approximate  $1/d$  dependence, as expected for thin superconducting films, and reaches 1.2 nH for the monolayer sample (see Supplementary Information for the determination of layer numbers). The values are compared to those of other superconductors based on amorphous materials, including TiN[22, 65], NbTiN[26, 27], granular aluminum (gr-Al)[61], and NbN[24] across a range of film thicknesses up to 13 nm, as shown in Fig. 4b. Notably, NbSe<sub>2</sub>, particularly in the few-monolayer regime, exhibits one of the highest sheet kinetic inductances reported at comparable thicknesses, surpassing those of many conventional high-impedance superconductors.

The observed layer dependence may provide insight into the underlying mechanisms responsible for the high  $L_k$ , including the role of scattering processes, and whether our NbSe<sub>2</sub> devices operate in the dirty limit, the clean limit, or an intermediate regime. We consider a general expression for the sheet kinetic inductance  $L_{k,\text{sq}}$  that spans from the clean to the dirty limit (see Supplementary Information for the derivation):

$$L_{k,\text{sq}} = \frac{1}{d} \left( \frac{m_{\text{eff}}}{n_0 e^2} + \frac{\hbar}{1.764 k_B T_c} \rho_s \right) = \frac{m_{\text{eff}}}{n_0 e^2 d} + \frac{\hbar}{1.764 k_B T_c} R_s \quad (2)$$

Here,  $\rho_s$  denotes the normal-state sheet resistivity,  $\hbar$  is the reduced Planck's constant,  $k_B$  is the Boltzmann constant, and  $R_s$  is the normal-state sheet resistance. If we assume that the term in parentheses varies slowly with film thickness, then we expect the approximate  $1/d$  dependence that we see in Fig. 4a. This expression suggests that the total kinetic inductance arises from a combination of clean-limit (first term)

and dirty-limit (second term) contributions. Figure 4c plots the measured sheet kinetic inductance  $L_{k,\text{sq}}$  as a function of  $R_s/T_c$ . The  $R_s$  and  $T_c$  values are obtained from both our transport measurements and previous studies (shown in green and black circles in Fig. 4c, summarized in Table S3). We observe a linear dependence for the larger values of  $L_{k,\text{sq}}$  in Fig. 4c. A linear fit yields a slope of 16.3 which characterizes the dirty-limit dependence, and the y-intercept of 80.0 pH shows that there is a significant contribution from the clean-limit for thicker samples (note that the  $1/d$  dependence for the clean-limit term can be considered, but qualitatively, the contribution from the clean-limit term remains significant). As the sample thickness approaches the monolayer limit, the ratio of the measured kinetic inductance to the clean-limit kinetic inductance ( $L_{k,\text{sq}}/L_{k,\text{sq},\text{clean}}$ ) increases from 0.7 to 15 monotonically, indicating that the dirty-limit contribution becomes increasingly significant in thinner NbSe<sub>2</sub> samples. This model captures the crossover from clean to the dirty-limit behavior as the sample thickness decreases.

We now discuss possible origins of the observed crossover behavior. In thicker NbSe<sub>2</sub> films, the majority of charge carriers reside in the interior layers of the 2D crystal. The clean-limit-like behavior observed in this regime—corresponding to the lower-left corner of Fig. 4c—may be attributed to the high crystallinity of the bulk material and effective screening from carriers in the top and bottom NbSe<sub>2</sub> layers. In contrast, thinner devices exhibit a greater influence from their surrounding environment. In the monolayer limit, all charge carriers are in close proximity to the encapsulating hBN on both sides, leading to enhanced surface scattering from impurities or fabrication residues. This increased scattering may result in more pronounced dirty-limit contributions to the kinetic inductance. Moreover, NbSe<sub>2</sub> has been shown to host two superconducting bands with distinct gap sizes, with the larger gap decreasing monotonically as thickness is reduced [63]. In other multi-band superconductors [66, 67], such disparity across the Fermi surface has been linked to the coexistence of clean- and dirty-limit behaviors, arising from band-dependent coherence lengths and scattering rates. Our experiment does not explicitly resolve contributions from individual bands, but similar multi-band effects may contribute to the observed layer dependence of kinetic inductance in NbSe<sub>2</sub> (Fig. 4c). Additionally, as the superconducting gap (or  $T_c$ ) decreases with reduced thickness, the superconducting coherence length becomes longer. For a fixed mean free path, this leads to a larger coherence length to mean free path ratio, indicating a shift toward dirty-limit behavior in the thinner samples. We note that the combined contributions from both clean- and dirty-limit superconductivity observed in the microwave measurements here contrast with previous DC transport studies, which reported only clean-limit behavior. This discrepancy suggests that the microwave response may be sensitive to the multi-band nature of NbSe<sub>2</sub> [41, 49–51].

Finally, in thin superconducting films where the thickness  $d$  is much smaller than the penetration depth  $\lambda$ ,

the relevant length scale becomes the Pearl length  $\Lambda = \frac{2\lambda^2}{d}$  [68]. All of our  $\text{NbSe}_2$  samples operate in this Pearl regime ( $d \ll \lambda \sim 230 \text{ nm}$  [69]), with both thickness and width much smaller than the estimated Pearl length (10-70  $\mu\text{m}$ ; see Supplementary Information). Recent studies on high- $T_c$  YBCO superconductors have shown that geometric confinement in this regime can strongly enhance the kinetic inductance as the device width approaches or falls below  $\Lambda$  [70]. While a detailed investigation of this effect in  $\text{NbSe}_2$  lies beyond the scope of this work, our observation of large  $L_k$  values — and a steeper-than-expected inverse thickness scaling, relative to the prediction of Eq. 2 — may be qualitatively consistent with such confinement-enhanced kinetic inductance in the Pearl regime.

## Conclusions

We characterize the kinetic inductance and nonlinear properties of  $\text{NbSe}_2$  using a coplanar waveguide resonator terminated by hBN-encapsulated  $\text{NbSe}_2$  thin films. The kinetic inductance shows an approximate  $1/d$ -type scaling for the thinner samples and reaches  $1.2 \text{ nH}/\square$  at monolayer thickness — among the highest reported for superconductors within this thickness regime. Under the microwave drive, the device exhibits a nonlinear frequency shift that is consistent with the nonlinear Kerr model. The extracted Kerr coefficients ( $K/2\pi = -0.008$  to  $14.7 \text{ Hz}/\text{photon}$ ) are relatively small, making  $\text{NbSe}_2$  well-suited for applications that require large linear inductance with minimal nonlinearity, such as the linear shunt-inductor used in fluxonium qubits and in photon detectors operating in the microwave regime [71]. The  $L_k$  exhibits a quadratic dependence on DC bias current, consistent with the Ginzburg-Landau framework.

The measured kinetic inductance in  $\text{NbSe}_2$  exhibits a crossover from clean- to dirty-limit behavior as the thickness decreases. This transition can be qualitatively described using a generalized expression for  $L_k$  derived from BCS theory. In the ultra-thin regime, enhanced contributions from the dirty limit may arise due to increased surface scattering, multi-band superconductivity, and geometric confinement.

We demonstrate that  $\text{NbSe}_2$  is a crystalline two-dimensional superconductor that exhibits large, linear inductance. The hBN- $\text{NbSe}_2$ -hBN heterostructure is well suited for compact lump-element devices, such as shunt inductors for fluxonium qubits or readout resonators, while minimizing parasitic coupling. These results also highlight the ability of microwave measurements to probe superconducting properties in low-dimensional materials, offering a valuable complement to DC transport and other techniques.

## Acknowledgements

The authors thank Shoumik D. Chowdhury, Aziza Almanakly, Lamia Ateshian, David Rower, Xirui Wang, Xueqiao Wang, and the device packaging team at MIT Lincoln Laboratory for their assistance in measurement, fabrication, and packaging. This work was carried out in part using the MIT.nano's facilities. This research was funded in part by the US Army Research Office grant no. W911NF-22-1-0023, by the National Science Foundation grant no. 2412810 and no. OMA-1936263, by the Air Force Office of Scientific Research grant no. FA2386-21-1-4058, and under Air Force Contract No. FA8702-15-D-0001. S.Z. acknowledges support from the Lisa Su (1990) Fellowship awarded by the EECS Department at MIT as well as the Faculty for the Future Fellowship from the Schlumberger Foundation. T. W. and P. K. acknowledge support from DOE contract DE-SC0012260. M.H. is supported by an appointment to the Intelligence Community Postdoctoral Research Fellowship Program at the Massachusetts Institute of Technology, administered by Oak Ridge Institute for Science and Education (ORISE) through an interagency agreement between the U.S. Department of Energy and the Office of the Director of National Intelligence (ODNI). D. R-L. acknowledges support from the Rafael del Pino Foundation. R.C. and A.K.D. acknowledge support from the U.S. Department of Energy, Office of Science National Quantum Information Science Research Center's Co-design Center for Quantum Advantage (C2QA) under contract number DE-SC0012704. R.C. and A.K.D. contributed to this work by performing low-frequency Raman spectroscopy measurements to determine the layer number/thickness of thin NbSe<sub>2</sub> flakes from shear-mode frequency analysis, and this contribution was supported by C2QA. K.W. and T.T. acknowledge support from the JSPS KAKENHI (Grant Numbers 21H05233 and 23H02052), the CREST (JPMJCR24A5), JST, and the World Premier International Research Center Initiative (WPI), MEXT, Japan. P.J-H. acknowledges support by the Air Force Office of Scientific Research (AFOSR) grant FA9550-21-1-0319, the Office of Naval Research (ONR) grant N000142412440, the MIT/Microsystem Technology Laboratories, Samsung Semiconductor Research Fund, the Gordon and Betty Moore Foundation's EPiQS Initiative through Grant No. GBMF9463, the Fundacion Ramon Areces, and the CIFAR Quantum Materials program. Any opinions, findings, conclusions, or recommendations expressed in this material are those of the author(s) and do not necessarily reflect the views of the U.S. Air Force or the U.S. Government.

## Author Contributions

J.Î-j.W. conceived and designed the experiment. S.Z., J.Î-j.W, and T.H.D. performed the microwave simulations. S.Z., T. W., M.T., J.Î-j.W., D. R-L., A.G., A.K.D., D.K.K., and B.M.N. contributed to the device

fabrication and characterization. S.Z., J.Î-j.W., T. W., R. A., M. H., and D. R-L participated in the measurements. S.Z., J.Î-j.W., R. A., and M.H. analyzed the data. K.W. and T.T. grew the hBN crystal. S.Z., J.Î-j.W., and W.D.O. led the paper writing, and all other authors contributed to the text. J.Î-j.W., J.A.G., K.S. M.E.S., R.C., P.K., P.J-H., T.P.O, and W.D.O supervised the project.

## **Competing Interests Statement**

The authors declare no competing interests.

Device ID	d (nm)	W (μm)	L (μm)	$f_{r,\text{Al-NbSe}_2}$ (GHz)	$f_{r,\text{Al}}$ (GHz)	$L_k$ (nH)	$L_{k,\text{sq}}$ (nH/sq)	$Q_{i,\text{Al-NbSe}_2}$	$K/2\pi$ (Hz)
D1	1.99	3.1	3.1	3.62	5.30	1.195	1.195	$0.8 \times 10^4$	-14.7
D2	4.08	2.5	5.7	4.14	5.21	0.643	0.282	$6.0 \times 10^4$	-3.8
D3	5.86	2.6	3.0	4.88	5.33	0.220	0.191	$0.7 \times 10^4$	-2.9
D4	7.13	4.8	6.7	4.93	5.35	0.200	0.143	$2.4 \times 10^4$	-2.6
D5	7.98	4.5	12.0	4.63	5.33	0.360	0.135	$1.2 \times 10^4$	-1.9
D6	8.81	3.9	8.6	4.79	5.34	0.274	0.124	$2.8 \times 10^4$	-1.7
D7	8.90	4.5	4.2	5.26	5.49	0.100	0.107	$2.1 \times 10^4$	-1.5
D8	10.07	2.5	6.6	5.16	5.49	0.149	0.056	$0.7 \times 10^4$	-0.4
D9	11.89	6.0	6.9	5.46	5.60	0.057	0.049	$0.6 \times 10^4$	-0.03
D10	24.73	4.1	7.5	5.34	5.37	0.014	0.008	$18 \times 10^4$	-0.006
D11	30.20	3.4	6.1	5.42	5.44	0.009	0.005	$2.5 \times 10^4$	-0.006
D12	52.12	2.3	4.6	5.6	5.62	0.008	0.004	$5.8 \times 10^4$	-0.008

Table 1: **Summary of kinetic microwave characterization of  $\text{NbSe}_2$  samples across different thicknesses.** W and L represent the nominal width and nominal length of the  $\text{NbSe}_2$  samples with a thickness of d.  $Q_{i,\text{Al-NbSe}_2}$  and Kerr coefficients ( $K/2\pi$ ) are extracted from  $\text{NbSe}_2$ -terminated Al resonators. The film thickness (d) is measured with atomic force microscopy (AFM).

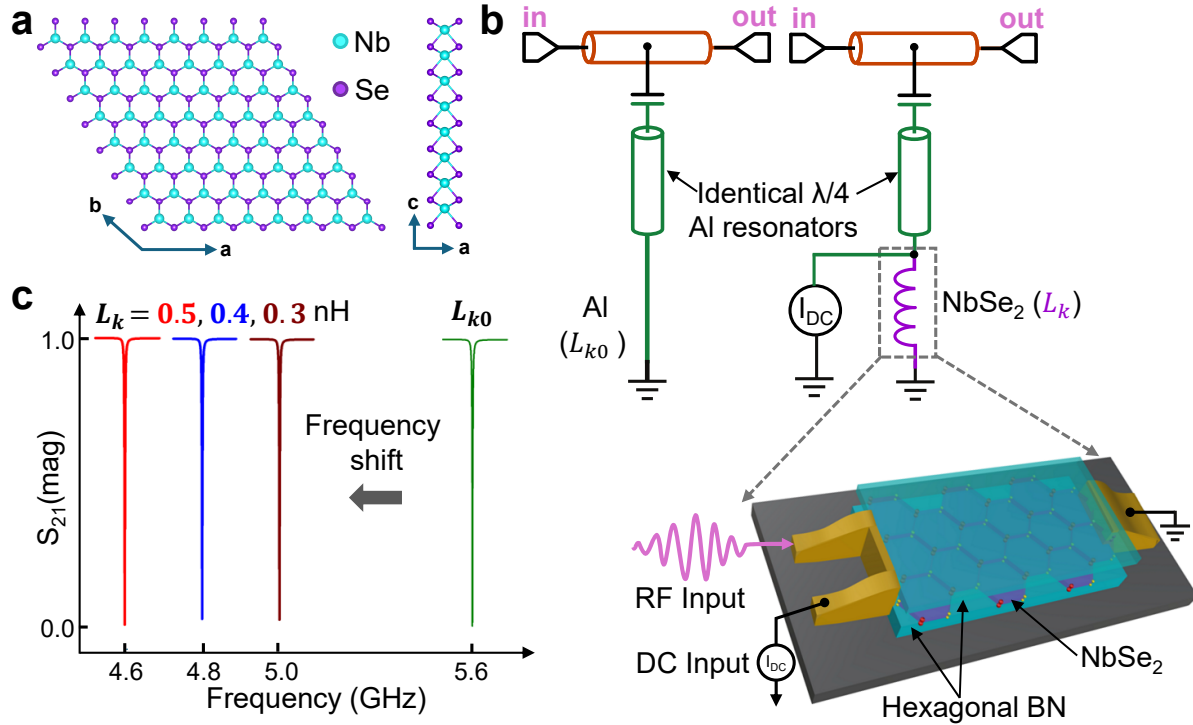


Figure 1: **Superconducting resonators and terminations to characterize the kinetic inductance of NbSe<sub>2</sub>.** **a**, Crystal structure of monolayer 2H-NbSe<sub>2</sub>, top-down and side views. **b**, Measurement circuit schematic. CPW resonators are capacitively coupled to a common transmission line and terminated either directly to ground via aluminum (control) or through a hBN-NbSe<sub>2</sub>-hBN heterostructure (experiment). The resonant frequency  $f_r$  of the aluminum  $\lambda/4$  resonator is determined by the effective inductance and capacitance of the CPW. Termination by NbSe<sub>2</sub> introduces additional kinetic inductance, shifting the resonant frequency to a new value  $f_{r'}$ . (Zoom-in of inductor) hBN-NbSe<sub>2</sub>-hBN heterostructure contacted by Al electrodes with both RF and DC input signals applied across the sample and terminated at ground. **c**, Simulated resonator spectra illustrating the effect of increased inductance on the resonant frequency.  $L_{k0}$  denotes the inductance of the aluminum-terminated resonator, while  $L_k$  represents the additional inductance introduced by the NbSe<sub>2</sub> sample.

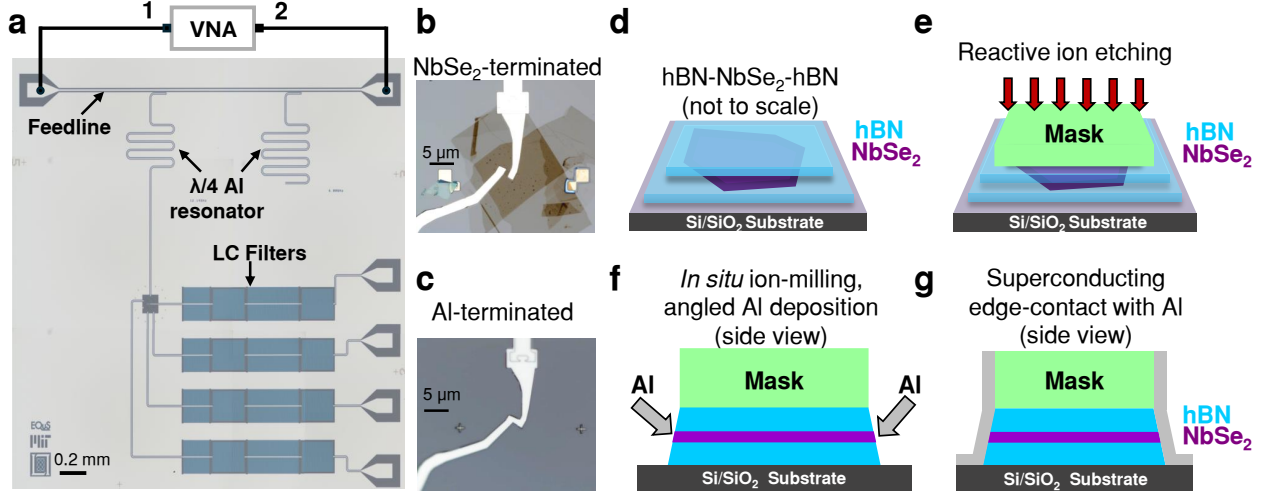
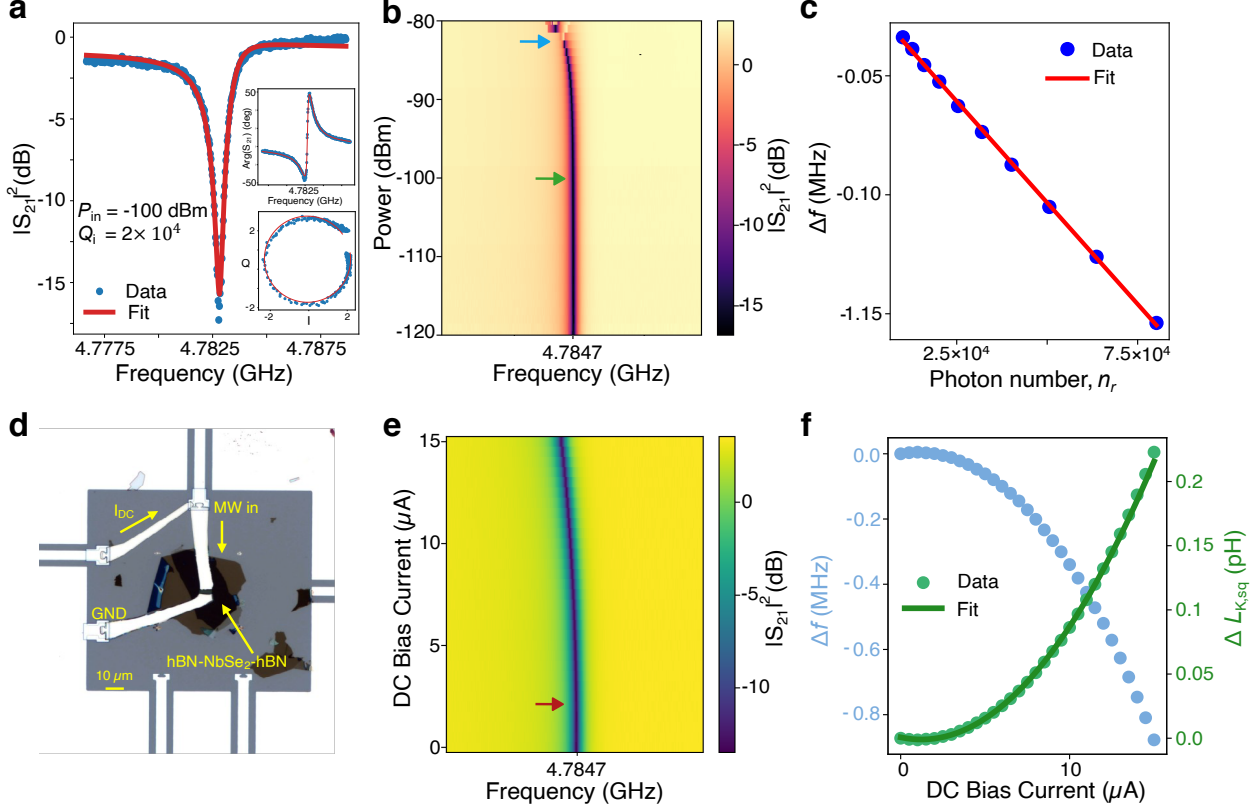


Figure 2: **Measurement configuration and device fabrication for the kinetic inductance measurement of  $\text{NbSe}_2$ .** **a**, Optical micrograph of a  $5 \times 5 \text{ mm}^2$  chip containing CPW resonators, a shared feedline, DC bias lines, on-chip LC filters, and a ground plane, all patterned from 250 nm-thick aluminum on a high-resistivity silicon substrate. Only one (of four) DC bias lines is used in this experiment. **b - c**, Optical micrographs of the  $\text{NbSe}_2$ -terminated and aluminum-terminated  $\lambda/4$  CPW resonators, respectively. **d - g**, Illustration of the edge-contact fabrication process. The  $\text{NbSe}_2$  (purple) flake is fully encapsulated by hBN (blue) and patterned via reactive-ion etching (RIE) to expose its edges. After in-situ argon ion milling, superconducting edge contacts are formed by angled aluminum evaporation with substrate rotation.



**Figure 3: Microwave measurements of  $\text{NbSe}_2$ -terminated  $\lambda/4$ -resonator.** **a**, Transmission coefficient ( $|S_{21}|$ ) of a  $\text{NbSe}_2$ -terminated  $\lambda/4$ -resonator measured at 10 mK (Device ID D6). Inset: Complex I–Q plane showing the measured response (blue) and Lorentzian fit (red). **b**, Transmission coefficient ( $|S_{21}|$ ) of  $\text{NbSe}_2$ -terminated  $\lambda/4$ -resonator resonator as a function of input microwave power ( $P_{rf}$ ). The resonant frequency ( $f_{r,\text{Al-NbSe}_2}$ ) shifts to the lower frequency with increasing microwave power. The onset of the frequency shift—defined as exceeding one standard deviation from the low-power baseline ( $f_{r,\text{Al-NbSe}_2} = 4.785 \text{ GHz}$ )—is observed at an input power of  $-100 \text{ dBm}$  (indicated by the green arrow). At  $-82 \text{ dBm}$ , the resonant peak bifurcates (blue arrow), indicating the onset of a bistable regime. **c**, Linear fit of the resonant frequency shift ( $\Delta f = f_{r,\text{Al-NbSe}_2}(n_r = 1) - f_{r,\text{Al-NbSe}_2}(n_r)$ ) as a function of resonator photon number ( $n_r$ ) in the  $\text{NbSe}_2$ -terminated  $\lambda/4$ -resonator. **d**, Optical image of the  $\text{NbSe}_2$ -terminated  $\lambda/4$ -resonator with a DC bias line connected at the microwave input port. **e**, DC bias dependence of the  $\text{NbSe}_2$ -terminated  $\lambda/4$ -resonator measured at a fixed microwave power of  $P_{rf} = -120 \text{ dBm}$ . The resonant frequency shifts to the lower frequency with increasing bias current. The onset of the frequency shift—defined as exceeding one standard deviation from the baseline ( $f_{r,\text{Al-NbSe}_2} = 4.785 \text{ GHz}$ )—is observed at a bias current of  $1 \mu\text{A}$  (maroon arrow). **f**, Extracted resonant frequency shift ( $\Delta f = f_{r,\text{Al-NbSe}_2}(I_{DC} = 0) - f_{r,\text{Al-NbSe}_2}(I_{DC})$ ) and kinetic inductance shift ( $\Delta L_{k,\text{sq}} = L_{k,\text{sq}}(I_{DC} = 0) - L_{k,\text{sq}}(I_{DC})$ ) of the  $\text{NbSe}_2$ -terminated resonator as a function of DC bias current. Measured data (circle-green and sky-blue) and theoretical fit (line-green) are shown.

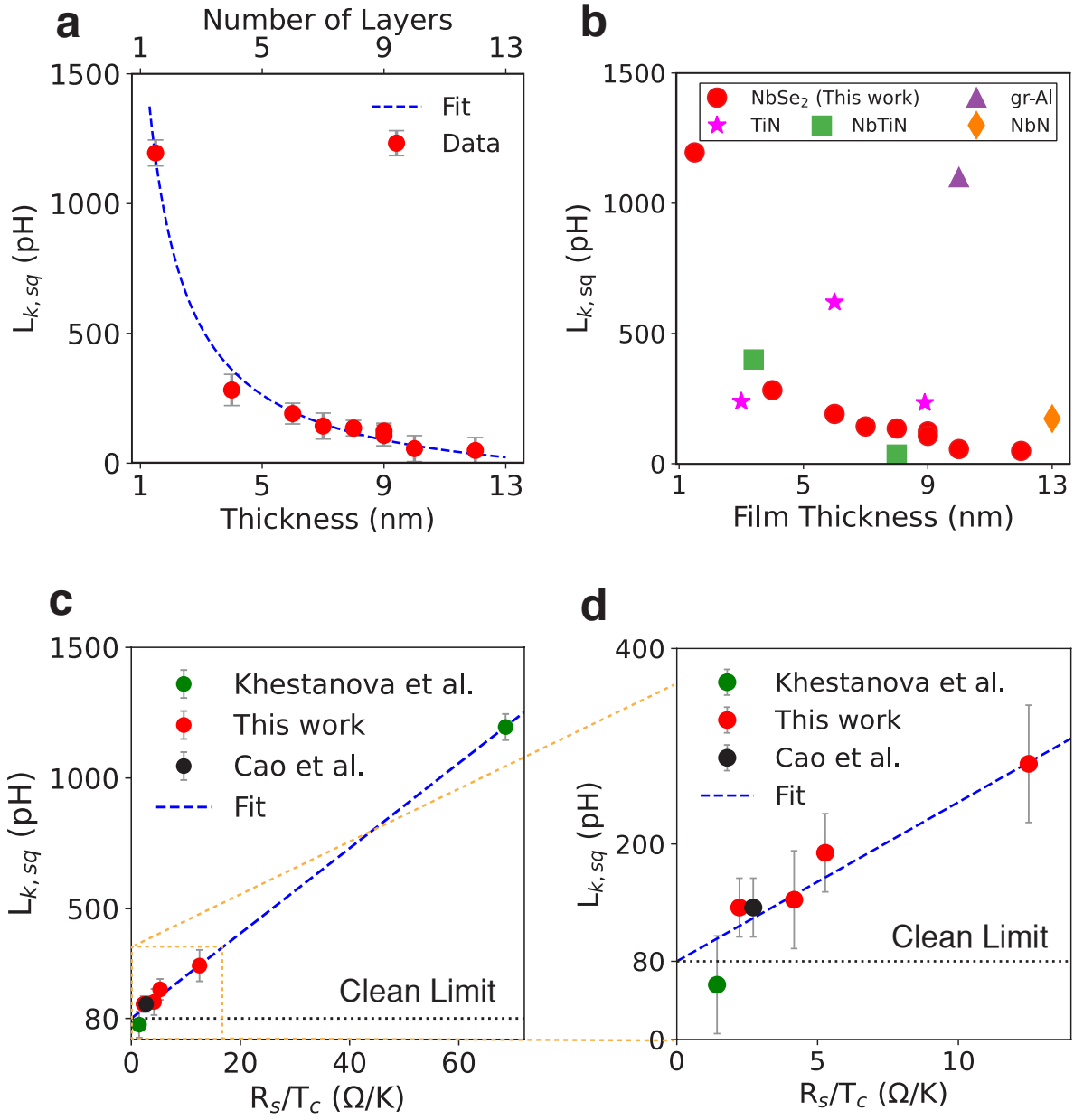


Figure 4: **Thickness dependence of kinetic inductance in NbSe<sub>2</sub>.** **a**, Sheet kinetic inductance ( $L_{k,\text{sq}}$ ) from microwave measurements (circle-red) of nine NbSe<sub>2</sub> devices with varying film thicknesses. The blue dashed line shows a  $1/d$  scaling fit. **b**, Comparison of measured  $L_{k,\text{sq}}$  in NbSe<sub>2</sub> with values reported for other high-impedance superconducting thin films [22, 24, 26, 27, 61, 65]. **c** Sheet kinetic inductance ( $L_{k,\text{sq}}$ ) from microwave measurements is plotted as a function of  $R_s/T_c$ , where  $R_s$  and  $T_c$  values are obtained from both our transport measurements (red circles) and previous studies (green and black circles)[41, 42]. The blue dashed line is a linear fit with a slope of 16.3 and a y-intercept of 80.0 pH, marked as the clean-limit contribution to  $L_{k,\text{sq}}$ . **d**, The magnified view of the lower region for clarity.

## References

1. Phan, D. *et al.* Detecting induced  $p\pm ip$  pairing at the Al-InAs interface with a quantum microwave circuit. *Physical Review Letters* **128**, 107701 (2022).
2. Böttcher, C. *et al.* Circuit quantum electrodynamics detection of induced two-fold anisotropic pairing in a hybrid superconductor–ferromagnet bilayer. *Nature Physics* **20**, 1609–1615 (2024).
3. Kreidel, M. *et al.* Measuring kinetic inductance and superfluid stiffness of two-dimensional superconductors using high-quality transmission-line resonators. *Physical Review Research* **6**, 043245 (2024).
4. Tanaka, M. *et al.* Superfluid stiffness of magic-angle twisted bilayer graphene. *Nature* **638**, 99–105 (2025).
5. Banerjee, A. *et al.* Superfluid stiffness of twisted trilayer graphene superconductors. *Nature* **638**, 93–98 (2025).
6. Jin, H. *et al.* Exploring van der Waals cuprate superconductors using a hybrid microwave circuit. *Nano Letters* **25**, 3191–3198 (2025).
7. Manucharyan, V. E., Koch, J., Glazman, L. I., Devoret, M. H., *et al.* Fluxonium: Single cooper-pair circuit free of charge offsets. *Science* **326**, 113–116 (2009).
8. Gynis, A. *et al.* Experimental realization of a protected superconducting circuit derived from the  $0-\pi$  qubit. *PRX Quantum* **2**, 010339 (2021).
9. Astafiev, O. *et al.* Coherent quantum phase slip. *Nature* **484**, 355–358 (2012).
10. Shaikhaidarov, R. S. *et al.* Quantized current steps due to the ac coherent quantum phase-slip effect. *Nature* **608**, 45–49 (2022).
11. Mi, X. *et al.* A coherent spin–photon interface in silicon. *Nature* **555**, 599–603 (2018).
12. Ye, Y. *et al.* Near-ultrastrong nonlinear light-matter coupling in superconducting circuits. *Nature Communications* **16**, 3799 (2025).
13. Puertas Martínez, J. *et al.* A tunable Josephson platform to explore many-body quantum optics in circuit-QED. *npj Quantum Information* **5**, 19 (2019).
14. Böttcher, C. *et al.* Parametric longitudinal coupling between a high-impedance superconducting resonator and a semiconductor quantum dot singlet-triplet spin qubit. *Nature Communications* **13**, 4773 (2022).
15. Clerk, A., Lehnert, K., Bertet, P., Petta, J., Nakamura, Y., *et al.* Hybrid quantum systems with circuit quantum electrodynamics. *Nature Physics* **16**, 257–267 (2020).
16. Landig, A. J. *et al.* Coherent spin–photon coupling using a resonant exchange qubit. *Nature* **560**, 179–184 (2018).

17. Mantegazzini, F. *et al.* High kinetic inductance NbTiN films for quantum limited travelling wave parametric amplifiers. *Physica Scripta* **98**, 125921 (2023).
18. Splitthoff, L. J. *et al.* Gate-tunable kinetic inductance parametric amplifier. *Physical Review Applied* **21**, 014052 (2024).
19. Macklin, C. *et al.* A near-quantum-limited Josephson traveling-wave parametric amplifier. *Science* **350**, 307–310 (2015).
20. Nguyen, L. B. *et al.* High-coherence fluxonium qubit. *Physical Review X* **9**, 041041 (2019).
21. Crescini, N. *et al.* Evidence of dual Shapiro steps in a Josephson junction array. *Nature Physics* **19**, 851–856 (2023).
22. Shearow, A. *et al.* Atomic layer deposition of titanium nitride for quantum circuits. *Applied Physics Letters* **113** (2018).
23. Amin, K. R. *et al.* Loss mechanisms in TiN high impedance superconducting microwave circuits. *Applied Physics Letters* **120** (2022).
24. Frasca, S. *et al.* NbN films with high kinetic inductance for high-quality compact superconducting resonators. *Physical Review Applied* **20**, 044021 (2023).
25. Niepce, D., Burnett, J., Bylander, J., *et al.* High kinetic inductance NbN nanowire superconductors. *Physical Review Applied* **11**, 044014 (2019).
26. Samkharadze, N. *et al.* High-kinetic-inductance superconducting nanowire resonators for circuit QED in a magnetic field. *Physical Review Applied* **5**, 044004 (2016).
27. Bretz-Sullivan, T. M. *et al.* High kinetic inductance NbTiN superconducting transmission line resonators in the very thin film limit. *Applied Physics Letters* **121** (2022).
28. Dupré, O. *et al.* Tunable sub-gap radiation detection with superconducting resonators. *Superconductor Science and Technology* **30**, 045007 (2017).
29. Calvo, M. *et al.* Niobium silicon alloys for kinetic inductance detectors. *Journal of Low Temperature Physics* **176**, 518–523 (2014).
30. Kirsh, N. *et al.* Linear and nonlinear properties of a compact high-kinetic-inductance WSi multimode resonator. *Physical Review Applied* **16**, 044017 (2021).
31. Zhang, W. *et al.* Microresonators fabricated from high-kinetic-inductance aluminum films. *Physical Review Applied* **11**, 011003 (2019).
32. Grünhaupt, L. *et al.* Loss mechanisms and quasiparticle dynamics in superconducting microwave resonators made of thin-film granular aluminum. *Physical Review Letters* **121**, 117001 (2018).
33. Glezer Moshe, A., Farber, E., Deutscher, G., *et al.* Granular superconductors for high kinetic inductance and low loss quantum devices. *Applied Physics Letters* **117** (2020).

34. Charpentier, T. *et al.* First-order quantum breakdown of superconductivity in an amorphous superconductor. *Nature Physics* **21**, 104–109 (2025).
35. Tinkham, M. *Introduction to superconductivity* (Courier Corporation, 2004).
36. Müller, C., Cole, J. H., Lisenfeld, J., *et al.* Towards understanding two-level-systems in amorphous solids: insights from quantum circuits. *Reports on Progress in Physics* **82**, 124501 (2019).
37. Arute, F. *et al.* Quantum supremacy using a programmable superconducting processor. *Nature* **574**, 505–510 (2019).
38. Kurilovich, V. D. *et al.* Correlated Error Bursts in a Gap-Engineered Superconducting Qubit Array. *arXiv preprint arXiv:2506.18228* (2025).
39. Xi, X. *et al.* Ising pairing in superconducting NbSe<sub>2</sub> atomic layers. *Nature Physics* **12**, 139–143 (2016).
40. De la Barrera, S. C. *et al.* Tuning Ising superconductivity with layer and spin-orbit coupling in two-dimensional transition-metal dichalcogenides. *Nature Communications* **9**, 1427 (2018).
41. Khestanova, E. *et al.* Unusual suppression of the superconducting energy gap and critical temperature in atomically thin NbSe<sub>2</sub>. *Nano Letters* **18**, 2623–2629 (2018).
42. Cao, Y. *et al.* Quality heterostructures from two-dimensional crystals unstable in air by their assembly in inert atmosphere. *Nano Letters* **15**, 4914–4921 (2015).
43. Du, Y. *et al.* Unveiling resilient superconducting fluctuations in atomically thin NbSe<sub>2</sub> through Higgs mode spectroscopy. *Physical Review Letters* **134**, 066002 (2025).
44. Benyamin, A. *et al.* Fragility of the dissipationless state in clean two-dimensional superconductors. *Nature Physics* **15**, 947–953 (2019).
45. Wan, P. *et al.* Orbital fulde–Ferrell–Larkin–ovchinnikov state in an ising superconductor. *Nature* **619**, 46–51 (2023).
46. Hamill, A. *et al.* Two-fold symmetric superconductivity in few-layer NbSe<sub>2</sub>. *Nature physics* **17**, 949–954 (2021).
47. Cho, C.-w. *et al.* Nodal and nematic superconducting phases in NbSe<sub>2</sub> monolayers from competing superconducting channels. *Physical Review Letters* **129**, 087002 (2022).
48. Tsen, A. *et al.* Nature of the quantum metal in a two-dimensional crystalline superconductor. *Nature Physics* **12**, 208–212 (2016).
49. Prober, D., Schwall, R., Beasley, M., *et al.* Upper critical fields and reduced dimensionality of the superconducting layered compounds. *Physical Review B* **21**, 2717 (1980).
50. Zhu, T. *et al.* Transport properties of few-layer NbSe<sub>2</sub>: From electronic structure to thermoelectric properties. *Materials Today Physics* **27**, 100789 (2022).

51. Benyamini, A. *et al.* Blockade of vortex flow by thermal fluctuations in atomically thin clean-limit superconductors. *arXiv preprint arXiv:1909.08469* (2019).
52. Maji, K. *et al.* Superconducting cavity-based sensing of band gaps in 2D materials. *Nano Letters* **24**, 4369–4375 (2024).
53. Wang, J. I. *et al.* Hexagonal boron nitride as a low-loss dielectric for superconducting quantum circuits and qubits. *Nature Materials* **21**, 398–403 (2022).
54. Dean, C. R. *et al.* Boron nitride substrates for high-quality graphene electronics. *Nature Nanotechnology* **5**, 722–726 (2010).
55. Sinko, M. R. *et al.* Superconducting contact and quantum interference between two-dimensional van der Waals and three-dimensional conventional superconductors. *Physical Review Materials* **5**, 014001 (2021).
56. Probst, S., Song, F., Bushev, P. A., Ustinov, A. V. & Weides, M. Efficient and robust analysis of complex scattering data under noise in microwave resonators. *Review of Scientific Instruments* **86** (2015).
57. Nayfeh, A. H., Mook, D. T., *et al.* *Nonlinear Oscillations* (John Wiley & Sons, 2008).
58. Lee, J. C., Oliver, W. D., Berggren, K. K. & Orlando, T. Nonlinear resonant behavior of a dispersive readout circuit for a superconducting flux qubit. *Physical Review B—Condensed Matter and Materials Physics* **75**, 144505 (2007).
59. Vijay, R., Devoret, M., Siddiqi, I., *et al.* Invited review article: The Josephson bifurcation amplifier. *Review of Scientific Instruments* **80** (2009).
60. Andersen, C. K. *et al.* Quantum versus classical switching dynamics of driven dissipative Kerr resonators. *Physical Review Applied* **13**, 044017 (2020).
61. Winkel, P. *et al.* Implementation of a transmon qubit using superconducting granular aluminum. *Physical Review X* **10**, 031032 (2020).
62. Weißl, T. *et al.* Kerr coefficients of plasma resonances in Josephson junction chains. *Physical Review B* **92**, 104508 (2015).
63. Dvir, T. *et al.* Spectroscopy of bulk and few-layer superconducting NbSe<sub>2</sub> with van der Waals tunnel junctions. *Nature Communications* **9**, 598 (2018).
64. Ugeda, M. M. *et al.* Characterization of collective ground states in single-layer NbSe<sub>2</sub>. *Nature Physics* **12**, 92–97 (2016).
65. Coumou, P. *et al.* Microwave properties of superconducting atomic-layer deposited TiN films. *IEEE transactions on applied superconductivity* **23**, 7500404–7500404 (2012).
66. Homes, C., Dai, Y., Wen, J., Xu, Z. & Gu, G. FeTe<sub>0.55</sub>Se<sub>0.45</sub>: A multiband superconductor in the clean and dirty limit. *Physical Review B* **91**, 144503 (2015).

67. Dai, Y. *et al.* Coexistence of clean-and dirty-limit superconductivity in LiFeAs. *Physical Review B* **93**, 054508 (2016).

68. Pearl, J. Current distribution in superconducting films carrying quantized fluxoids. *Applied Physics Letters* **5**, 65 (1964).

69. Fridman, N. *et al.* Anomalous thickness dependence of the vortex pearl length in few-layer NbSe<sub>2</sub>. *Nature Communications* **16**, 2696 (2025).

70. Srivastava, Y. K. *et al.* YBa<sub>2</sub>Cu<sub>3</sub>O<sub>7</sub> as a high-temperature superconductor. *Nature Materials*, 1–8 (2025).

71. Shein, K. *et al.* Fundamental limits of few-layer NbSe<sub>2</sub> microbolometers at terahertz frequencies. *Nano Letters* **24**, 2282–2288 (2024).

72. Wang, J. I.-J. *et al.* Coherent control of a hybrid superconducting circuit made with graphene-based van der Waals heterostructures. *Nature Nanotechnology* **14**, 120–125 (2019).

73. Wang, L. *et al.* One-dimensional electrical contact to a two-dimensional material. *Science* **342**, 614–617 (2013).

74. Pizzocchero, F. *et al.* The hot pick-up technique for batch assembly of van der Waals heterostructures. *Nature Communications* **7**, 11894 (2016).

75. Grünhaupt, L. *et al.* An argon ion beam milling process for native AlOx layers enabling coherent superconducting contacts. *Applied Physics Letters* **111** (2017).

76. Sanna, A. *et al.* Real-space anisotropy of the superconducting gap in the charge-density wave material 2H-NbSe<sub>2</sub>. *npj Quantum Materials* **7**, 6 (2022).

77. Yokoi, M. *et al.* Negative resistance state in superconducting NbSe<sub>2</sub> induced by surface acoustic waves. *Science Advances* **6**, eaba1377 (2020).

78. Baity, P. G. *et al.* Circle fit optimization for resonator quality factor measurements: Point redistribution for maximal accuracy. *Physical Review Research* **6**, 013329 (2024).

79. Reagor, M. J. *Superconducting cavities for circuit quantum electrodynamics* (Yale University, 2016).

80. Yurke, B., Buks, E., *et al.* Performance of cavity-parametric amplifiers, employing Kerr nonlinearities, in the presence of two-photon loss. *Journal of Lightwave Technology* **24**, 5054–5066 (2006).

81. Norris, G. J. *et al.* Improved parameter targeting in 3D-integrated superconducting circuits through a polymer spacer process. *EPJ Quantum Technology* **11**, 5 (2024).

82. Pozar, D. M. *Microwave Engineering* (John Wiley & Sons, 2011).

83. Parks, R. & Tinkham, M. *Superconductivity Vols. 1, 2* 1970.

84. Orlando, T. P. & Delin, K. A. *Foundations of Applied Superconductivity* (Addison-Wesley, 1991).

85. Orlando, T., McNiff Jr, E., Foner, S. & Beasley, M. Critical fields, Pauli paramagnetic limiting, and material parameters of Nb<sub>3</sub>Sn and V<sub>3</sub>Si. *Physical Review B* **19**, 4545 (1979).

86. Xi, X. *et al.* Strongly enhanced charge-density-wave order in monolayer NbSe<sub>2</sub>. *Nature Nanotechnology* **10**, 765–769 (2015).
87. He, R. *et al.* Interlayer breathing and shear modes in NbSe<sub>2</sub> atomic layers. *2D Materials* **3**, 031008 (2016).
88. Lui, C. H., Ye, Z., Keiser, C., Xiao, X., He, R., *et al.* Temperature-activated layer-breathing vibrations in few-layer graphene. *Nano Letters* **14**, 4615–4621 (2014).

## Data availability

The data that support the findings of this study are available from the corresponding author upon reasonable request and with the cognizance of our US Government sponsors, who funded the work.

# Supplementary Information

## Contents

<b>1</b>	<b>Device Assembly and Fabrication</b>	<b>23</b>
<b>2</b>	<b>Optimization of the Contact Resistance between hBN encapsulated NbSe<sub>2</sub> and Al</b>	<b>24</b>
<b>3</b>	<b>Measurement Setup</b>	<b>25</b>
<b>4</b>	<b>Resonator Circular Fit</b>	<b>26</b>
<b>5</b>	<b>Non-linearity of the Resonator from the Inductance</b>	<b>26</b>
<b>6</b>	<b>Extraction of Kinetic Inductance from Resonance Frequency</b>	<b>28</b>
<b>7</b>	<b>Kinetic inductance: Clean and Dirty Limits</b>	<b>29</b>
7.1	Clean Limit . . . . .	29
7.2	Dirty Limit . . . . .	30
7.3	Full range calculation: from clean to dirty limit . . . . .	31
<b>8</b>	<b>Pearl Length</b>	<b>32</b>
<b>9</b>	<b>Determination of NbSe<sub>2</sub> Thickness and Layer Number</b>	<b>32</b>
9.1	AFM characterization of hBN-NbSe <sub>2</sub> -hBN stack . . . . .	32
9.2	Raman Spectroscopy of thin NbSe <sub>2</sub> films . . . . .	32

## 1 Device Assembly and Fabrication

Aluminum CPW resonators are fabricated from a highly resistive 2-inch Si wafer coated with 250 nm MBE-grown aluminum film. The resonator circuit is patterned via photolithography and wet etched using Transene Aluminum etchant. Afterwards, the 2-inch wafer is diced into 5 mm by 5 mm chips. The bulk crystal of NbSe<sub>2</sub> is grown by HQ Graphene. The mechanical exfoliation and encapsulation of thin NbSe<sub>2</sub> layers with hBN are carried out inside an Argon-filled glove box, maintaining oxygen and water levels below 0.1 ppm. This prevents oxidation of NbSe<sub>2</sub>, keeping the devices within the low-disorder regime. The hBN-NbSe<sub>2</sub>-hBN heterostructures are transferred on the chip using dry polymer-based techniques [72–74]. After transferring the hBN-NbSe<sub>2</sub>-hBN stacks onto the pre-patterned chips, the van der Waals heterostructures are taken out

of the glove box. To process edge-contact, first the stack goes through reactive-ion etching with  $O_2/Ar/CHF_3$  to open edges of  $NbSe_2$ . The samples are immediately loaded into an e-beam evaporator to do in-situ ion-milling to clean the exposed edges. Aluminum is then deposited onto the cleaned  $NbSe_2$  edge at a tilt angle of  $30^\circ$  with the substrate rotating at 60 rpm, ensuring uniform coverage [55]. The bridging between the contact aluminum and the pre-fabricated aluminum resonator and ground plane is done by another in-situ ion mill and a normal aluminum deposition [75].

## 2 Optimization of the Contact Resistance between hBN encapsulated $NbSe_2$ and Al

It is critical to establish a low-resistance, transparent contact (with near-zero contact resistance) between hBN encapsulated  $NbSe_2$  and the aluminum electrode for achieving impedance matching and accurate resonant frequency measurements. A low contact resistance ( $R_c$ ) is required because if it exceeds the characteristic impedance ( $50\Omega$  for our case), the resonator behaves like a  $\lambda/2$ -resonator instead of the desired  $\lambda/4$  mode terminated with  $NbSe_2$  sample. This happens because the higher resistance causes the end of the resonator to act like an open circuit, disrupting the intended resonant behavior. Additionally, minimizing  $R_c$  reduces dissipation and enables high-Q, high-accuracy measurements for characterizing the kinetic inductance and other superconducting properties of  $NbSe_2$ .

We fabricate a few devices for DC measurement using the above fabrication procedures to confirm a reliable superconducting contact between thin  $NbSe_2$  and Al. We vary the ion-milling duration to determine the optimal time needed to remove oxides from the edges of  $NbSe_2$ . To eliminate the line resistances, we measure the devices in a pseudo-4-probe configuration, Fig. S1a. Below the transitions of both  $NbSe_2$  and Al, the total resistance of the device, including the Al- $NbSe_2$  junctions, drops to zero within the noise floor of our measurement ( $R_c = 0.01\Omega$ ) Fig. S1b-c. We present the results of the measurement of DC contact devices to optimize the contact resistance as a function of the ion milling time. The results are summarized in the Table S1. We chose the optimum ion milling time of 105 seconds for our microwave devices presented in the main text. The bulk  $NbSe_2$  undergoes a transition into the charge-order phase at  $T \sim 33\text{ K}$ , and a transition into the superconducting phase at  $T \sim 7\text{ K}$  [42, 46, 76]. As the thickness of  $NbSe_2$  decreases, the critical temperature ( $T_c$ ) decreases, as shown in Fig. S1d, our results are consistent with other studies in the literature [41]. All our  $NbSe_2$  samples are high-quality crystals with relatively high residual resistance ratios ( $R_{300\text{K}}/R_N = 5\text{-}10$ ) [46], the normal-state sheet resistance ( $R_s$ ) right above the superconducting transition increases as the thickness of  $NbSe_2$  decreases; the values are summarized in Table S1. Figure S1e-f

<b>Ion-milling time (sec)</b>	<b><math>R_c</math> (<math>\Omega/\mu\text{m}</math>)</b>	<b><math>R_s</math> (<math>\Omega/\text{sq}</math>)</b>	<b><math>T_c</math> (K)</b>	<b>d (nm)</b>
120	0.01	N/A	N/A	10
105	0.01	31	5.5	6
90	0.01	19	7	8
90	0.02	N/A	N/A	4
80	1,80	60	4.8	4
75	0.02,2	29	5.5	6
60	0.02	45	4.9	5

Table S1: **Summary of DC samples for contact resistance characterization.** The in-situ ion-milling time and the thickness of  $\text{NbSe}_2$  both have been varied to characterize the contact resistance between  $\text{NbSe}_2$  edge and aluminum interface.

shows four-terminal transport characterization of one of the devices ( $d = 8 \text{ nm}$ ) using current biasing. The differential resistance was measured by applying a small AC excitation current (1 nA) superimposed on a DC bias current and detecting the AC voltage ( $dV$ ) between two electrodes. The critical current of the  $\text{NbSe}_2$  sample is of order 0.4 mA, which is consistent with the previous study [71, 77].

### 3 Measurement Setup

Figure S2 shows the wiring diagram of the measurement setup used for this work. To send the microwave signals down to the package, we use semi-rigid coaxial cables with low thermal conductivity and low-loss superconducting niobium-titanium (NbTi) cables for the readout. Within our readout input lines, we have integrated attenuation mechanisms: a 20 dB attenuator at 4 K, a 20 dB attenuator at the still plate, and a 30 dB attenuator at the mixing chamber stage. The output signals pass through a 2 GHz high-pass filter and a 12 GHz low-pass filter. We have a Josephson traveling-wave parametric amplifier (TWPA) in our read-out chain, and the TWPA pump tone is combined with the readout signal using a directional coupler, and the signal undergoes a final amplification stage employing a low-noise high-electron-mobility transistor (HEMT) amplifier positioned at the 4 K stage and a room temperature amplifier. DC lines connected to the device are filtered at 4 K with an RC  $\pi$ -filter and an RF+RC filter with a cut-off frequency of 50 kHz at the mixing chamber stage. The control electronics used in this experiment are listed in the Table S2.

Component	Manufacturer	Model
Dilution Refrigerator	Bluefors	XLD1000
VNA	Keysight	N5232A
DC Source	QDevil	QDAC
Lock-in Amplifier	Stanford Research Systems	SR830
Multimeter	Keithley	2010

Table S2: **Summary of control electronics.** Specifications of the control equipment used in the experiment, with their manufacturer and Model numbers.

## 4 Resonator Circular Fit

For notch-type geometry, where the resonator is coupled to a transmission line, the frequency-dependent transmission  $S_{21}$  is given by [56, 78]:

$$S_{21}^{notch}(f) = ae^{i\alpha} e^{-2\pi if\tau} \left[ 1 - \frac{\left(\frac{Q_L}{|Q_c|}\right) e^{i\phi}}{1 + 2iQ_L \left(\frac{f}{f_r} - 1\right)} \right] \quad (3)$$

where  $f$  is the signal frequency,  $f_r$  is the resonance frequency,  $Q_L$  is the loaded quality factor,  $Q_c$  is the coupling quality factor, and  $\phi$  corresponds to the phase shift of resonance due to the impedance mismatch with the transmission line. The prefactor ( $ae^{i\alpha}$ ) includes the overall gain and phase delay of the transmission line, including all the attenuation and amplification. Additionally,  $\tau$  denotes the propagation time in the transmission line, which introduces a phase shift proportional to the frequency  $f$ . Figure S3 shows the raw data (blue) and the Lorentzian fit using Eq. 3 (red) of the spectator resonator in the single-photon limit. We extract the values of the loaded quality factor ( $Q_L$ ) and the coupling quality factor ( $Q_c$ ) from the fit. The internal loss determines the intrinsic quality ( $Q_i$ ) of the resonator extracted from:  $\frac{1}{Q_L} = \frac{1}{Q_i} + \frac{1}{Q_c}$ . The fitted internal quality factors ( $Q_i$ ) of six different  $\lambda/4$ -resonators are plotted in Fig. S4c.

## 5 Non-linearity of the Resonator from the Inductance

We observe the resonant frequency shift in the  $\text{NbSe}_2$ -terminated resonator at higher microwave power (Fig. 3, main text), while the Al-terminated resonator does not show this behavior (Fig. S4b). The resonant frequency shift with increasing photon number in the resonator is described by the Kerr Hamiltonian [57, 79, 80]

$$H = \hbar\omega_r a^\dagger a + \frac{\hbar}{2} K a^\dagger a^\dagger a a \quad (4)$$

where  $\hbar$  is the reduced Planck constant,  $a$  and  $a^\dagger$  are the creation and the annihilation operators,  $\omega_r$  is the resonant frequency, and  $K$  is the Kerr constant, which is a measure of the strength of the nonlinearity in the system. The Kerr nonlinearity shifts the resonance frequency and is proportional to the resonator photon number. In addition to the power-dependent frequency shift, we observe a broadening of the internal linewidth as the number of photons in the cavity increases. The Kerr coefficient of  $\text{NbSe}_2$  is determined by analyzing the relationship between the resonance frequency shift ( $\Delta f$ ) and the resonator photon number ( $n_r$ ) in the resonator. We calculate the photon number in the resonator as a function of the applied power using the following formula [81],

$$n_r = \frac{2\kappa P_{\text{rf}}}{\hbar\omega_r(\kappa + \gamma)^2} \quad (5)$$

Here,  $\kappa$  represents the coupling rate to the feedline,  $P_{\text{rf}}$  is the power applied at the resonator input, and  $\gamma$  is the internal loss rate.

Expanding the current-dependent kinetic inductance relation of Eq. 1 (main text), the quartic energy contribution is expressed as

$$U_m = \frac{1}{2} L_k \frac{I_{\text{DC}}^4}{I^{*2}} \quad (6)$$

Here,  $I^*$  sets the scale for the non-linearity of the film. Applying circuit quantization, the current operator can be expanded in terms of ladder operators as  $\hat{I}_{\text{DC}} = I_{\text{zpf}}(a + a^*)$  where  $I_{\text{zpf}} = \sqrt{\frac{\hbar\omega_r}{2L_0}}$  is the zero-point current fluctuation of the mode and  $L_0$  is the total inductance of the resonator mode. We obtain the quantized nonlinear energy term of Eq. 6 as

$$\hat{U}_m = \frac{1}{2} L_k \frac{I_{\text{zpf}}^4}{I^{*2}} (a + a^*)^4 \quad (7)$$

The Kerr nonlinearity arises from the term proportional to  $a^*a^*aa$  in the quartic expansion, and the resulting Kerr coefficient ( $K$ ) is

$$K = \frac{6L_k I_{\text{zpf}}^4}{\hbar I^{*2}} = \frac{3\hbar\omega_r^2}{2L_0^2} \cdot \frac{L_k}{I^{*2}} \quad (8)$$

For device D6 (shown in Fig. 3 of the main text), we calculate the Kerr coefficient to be  $K/2\pi = -3.8$  Hz/photon using Eq. 8, which is in good agreement with the value ( $K/2\pi = -1.7$ ) extracted from the power-dependent frequency shift. The calculation uses  $f_{\text{r,Al-NbSe}_2} = 4.79$  GHz,  $L_0 = L_g + L_k = 2.627$  nH,

and  $I^* = 0.4 \text{ mA}$ .

## 6 Extraction of Kinetic Inductance from Resonance Frequency

To extract the kinetic inductance ( $L_k$ ) of  $\text{NbSe}_2$ , we employ a comparative model using  $\lambda/4$ -resonators terminated with aluminum and  $\text{NbSe}_2$ . For the aluminum-terminated resonator with a length of  $l$  and a resonant frequency of  $f_{r,Al}$ , the input impedance  $Z_{Al}$  is expressed as [82]

$$Z_{Al,in} = Z_0 \tanh(\alpha + i\beta)l \quad (9)$$

where,  $Z_0$  is the characteristic impedance which is  $50 \Omega$  in our work,  $\alpha$  and  $\beta$  are the attenuation constant and phase constant respectively. For a lossless line, the attenuation constant  $\alpha$  is zero, and  $\beta(f)$  becomes

$$\beta(f) = \frac{2\pi f_{r,Al} \sqrt{\epsilon_{eff}}}{c} \quad (10)$$

where  $\epsilon_{eff}$  is the effective permittivity of the substrate (Si), and  $c$  is the speed of light in vacuum. Assuming a low-loss transmission line, we take  $\alpha = 0$ , so that the input impedance simplifies to  $Z_{Al,in} = iZ_0 \tan(\beta l)$ . On resonance,  $\beta l = \pi/2$ , which yields the resonant frequency of the Al-terminated resonator  $f_{r,Al} = \frac{c}{4l\sqrt{\epsilon_{eff}}}$ .

For the  $\lambda/4$ -resonator terminated by  $\text{NbSe}_2$ , the kinetic inductance ( $L_k$ ) contributes an additional frequency-dependent term in the impedance, which is modeled as,

$$Z_{Al-\text{NbSe}_2,in} = Z_0 \frac{i\omega_{r,Al-\text{NbSe}_2} L_k + Z_0 \tanh(i\beta l)}{Z_0 + i\omega_{r,Al-\text{NbSe}_2} L_k \tanh(i\beta l)} \quad (11)$$

The physical length  $l$  of the resonator is determined from the aluminum reference resonator using Eq. 9, assuming identical geometry and effective permittivity. On resonance, the impedance of a  $\lambda/4$ -resonator diverges; for the  $\text{NbSe}_2$ -terminated case, Eq. 11 reduces to

$$\tan\left(\frac{\omega_{r,Al-\text{NbSe}_2} \sqrt{\epsilon_{eff}}}{c} l\right) = \frac{Z_0}{\omega_{r,Al-\text{NbSe}_2} L_k} \quad (12)$$

We extract the kinetic inductance  $L_k$  of  $\text{NbSe}_2$  from Eq. 12, where the resonant frequency of  $\text{NbSe}_2$ -terminated resonator is in the linear regime (in the single-photon limit).

## 7 Kinetic inductance: Clean and Dirty Limits

The purity of a superconductor is characterized by the ratio of the mean free path ( $l_{\text{MFP}}$ ) of the Cooper pairs to the BCS coherence length ( $\xi_0$ ). The mean free path ( $l_{\text{MFP}}$ ) is defined as  $l_{\text{MFP}} = \tau v_F$  with  $\tau$  representing the time interval between collisions in the normal state of the superconductor and  $v_F$  denoting the Fermi velocity [35]. The superconductor is in the dirty metal limit if the mean free path ( $l_{\text{MFP}}$ ) is much shorter than the BCS coherence length ( $\xi_0$ ), and in the clean limit if  $l_{\text{MFP}}$  is much longer than  $\xi_0$  [83]. To obtain kinetic inductance for both the dirty and clean limit, two pieces of information are required: (1) the generalized first London equation for a superconductor relating current density and electric field, and (2) an expression characterizing the penetration depth (specifically in the dirty/clean limit). The first London equation establishes a direct relation between the supercurrent density ( $\vec{J}$ ) and the electric field ( $\vec{E}$ ),

$$\frac{\partial \vec{J}}{\partial t} = \frac{1}{\mu_0 \lambda^2} \vec{E} \quad (13)$$

where  $\lambda$  is the penetration depth and  $\mu_0$  is the permeability of free space. When combined with Maxwell's equations, the London formalism further predicts that magnetic fields decay exponentially inside a superconductor, with the characteristic length  $\lambda$ . With a sinusoidal drive of frequency  $\omega$ , Eq. 13 gives

$$i\omega (\mu_0 \lambda^2) J = E \quad (14a)$$

$$i\omega \left( \mu_0 \lambda^2 \frac{l}{A} \right) I = V \quad (14b)$$

Equation 14b follows from the substitutions  $V = El$  and  $I = JA$ , and the prefactor in the parentheses represents the kinetic inductance.

$$L_k = \mu_0 \lambda^2 \frac{l}{A} \quad (15)$$

Equation 15 depends on the phenomenological parameter  $\lambda$ , which needs to be evaluated in both clean and dirty limits.

### 7.1 Clean Limit

In the clean limit, where the mean free path of the superconducting carriers is much longer than the coherence length, scattering events can be neglected. In this case, the dynamics of the supercurrent are determined

solely by the acceleration of Cooper pairs under the applied electric field. This leads to the relation

$$\frac{d}{dt}(m_{\text{eff}}\vec{v}) = \frac{d}{dt}\left(\frac{m_{\text{eff}}}{n_0e^2}\vec{J}\right) = \vec{E} \quad (16)$$

Here,  $n_0$  is the carrier density and  $m_{\text{eff}}$  is the effective mass of the supercurrent carriers. Equation 16 allows us to identify the penetration depth ( $\lambda_{\text{clean}}$ ) and kinetic inductance ( $L_{k,\text{clean}}$ ) in the clean limit as,

$$\mu_0\lambda_{\text{clean}}^2 = \frac{m_{\text{eff}}}{n_0e^2} \quad (17)$$

$$L_{k,\text{clean}} = \frac{m_{\text{eff}}}{n_0e^2} \left(\frac{l}{A}\right) \quad (18)$$

This penetration depth is known as the London penetration depth ( $\lambda_{\text{clean}} = \lambda_L$ ).

## 7.2 Dirty Limit

In the dirty limit, impurity scattering shortens the mean free path of the carriers, which weakens superfluid screening and causes the magnetic field to penetrate deeper, leading to an enhanced penetration depth given by [35, 84],

$$\lambda_{\text{dirty}} \approx \lambda_L \left(\frac{\xi_0}{l_{\text{MFP}}}\right)^{1/2} \quad (19)$$

where  $\xi_0$  is the BCS coherence length at zero temperature ( $\xi_0 = \frac{\hbar v_F}{\pi\Delta_0} = \xi_{\text{clean}}$ ) and the coherence length in the dirty limit becomes,

$$\xi_{\text{dirty}} \approx \xi_0 \left(\frac{l_{\text{MFP}}}{\xi_0}\right)^{1/2} = (\xi_0 l_{\text{MFP}})^{1/2} \quad (20)$$

Plugging the expression of  $\lambda_{\text{dirty}}$  into the general expression for  $L_k$  in Eq. 15, we get

$$L_{k,\text{dirty}} = \mu_0\lambda_{\text{dirty}}^2 \frac{l}{A} = \mu_0\lambda_L^2 \left(\frac{\xi_0}{l_{\text{MFP}}}\right) \frac{l}{A} \quad (21)$$

Now, using the expression of the BCS coherence length ( $\xi_0 = \hbar v_F/\pi\Delta_0$ ) and London penetration depth ( $\lambda_L$ ), we obtain

$$L_{k,\text{dirty}} = \frac{m_{\text{eff}}}{n_0e^2} \frac{\hbar v_F}{\pi\Delta_0} \frac{l}{l_{\text{MFP}} A} \quad (22)$$

Equation 22 can be further simplified by substituting the expressions for mean free path ( $l_{\text{MFP}} = v_F\tau$ ) and resistivity ( $\rho_s = 1/\sigma$ ).

$$L_{k,\text{dirty}} = \rho_s \frac{\hbar}{\pi\Delta_0} \frac{l}{A} = R_s \frac{\hbar}{\pi\Delta_0} \frac{l}{w} \quad (23)$$

where  $R_s$  is the normal-state sheet resistance of a current-carrying superconducting wire of length  $l$ , width  $w$ , and film thickness  $d$ . The BCS superconducting gap is approximated to  $\Delta_0 \approx 1.764k_B T_c$  for  $T \ll T_c$  with  $T_c$  the critical temperature and Eq. 23 becomes

$$L_{k,sq,dirty} = \frac{\hbar}{1.764k_B} \frac{R_s}{T_c} \quad (24)$$

Layers	$L_{k,sq}$ (pH/sq)	$T_c$ (K)	$R_s$ ( $\Omega$ /sq)	$R_s/T_c$ ( $\Omega/K$ )	$L_{k,sq}/L_{k,sq,clean}$
1	1195	3.5 <sup>[41]</sup>	240 <sup>[41]</sup>	68.57	14.95
4	282	4.8	60	12.5	3.53
6	191	5.5	29	5.27	2.39
7	143	6.0	25	4.17	1.79
8	135	7	19	2.71	1.79
8	135	6.3 <sup>[42]</sup>	14 <sup>[42]</sup>	2.22	1.75
10	56	7.0 <sup>[41]</sup>	10 <sup>[41]</sup>	1.43	0.71

Table S3: **Kinetic inductance of  $\text{NbSe}_2$  from clean to dirty limit**

### 7.3 Full range calculation: from clean to dirty limit

We can calculate the kinetic inductance for arbitrary  $\xi_0/l_{MFP}$  (where the ratio of  $\xi_0/l_{MFP}$  is of the order of 1). The Ginzburg-Landau theory gives a penetration depth of the form which can be well approximated by (Eq. 3.123b in [35] and the appendix in [85]):

$$\lambda = \lambda_L \left( 1 + a \frac{\xi_0}{l_{MFP}} \right)^{1/2} \quad (25a)$$

$$L_k = \mu_0 \lambda_L^2 \left( 1 + a \frac{\xi_0}{l_{MFP}} \right) \left( \frac{l}{A} \right) \quad (25b)$$

$$L_{k,sq} = \mu_0 \frac{\lambda_L^2}{d} + \mu_0 \frac{\lambda_L^2}{d} \left( a \frac{\xi_0}{l_{MFP}} \right) \quad (25c)$$

The factor  $a$  in Eq. 25a-c is the order of unity ( $a = 0.75$ ), but we have set  $a$  to be unity in the main text for simplicity. Equation 25c indicates that the kinetic inductance per square is the sum of the clean and dirty limit results. We can extract the ratio of coherence length to mean free path ( $\frac{\xi_0}{l_{MFP}}$ ) from the above expression.

$$\frac{\xi_0}{l_{MFP}} = \frac{L_{k,sq}}{L_{k,sq,clean}} - 1 \quad (26)$$

Figure S5 shows the clean- and dirty-limit contributions to the measured sheet kinetic inductance  $L_{k,sq}$  of  $\text{NbSe}_2$  samples, highlighting the  $1/d$  dependence of the clean-limit term in thicker samples and the dominant dirty-limit contributions in thinner samples.

Figure S5 plots results from the second expression in Eq. 2 which is of the form  $L_{k,\text{sq}} = A/d + (\hbar 1.764k_B)R_s/T_c$ . Figure S5a plots  $L_{k,\text{sq}} \times d$  versus  $\rho/T_c$  where  $\rho = R_s d$ . The y-intercept of Fig. S5a is used to get an estimate of  $A$ . Figure S5b uses this value of  $A$  to plot,  $L_{k,\text{sq}} - A/d$  versus  $R_s/T_c$ , where the y axis now shows the contribution to  $L_{k,\text{sq}}$  from the dirty limit. Given that  $A/d$  is about 70 pH for the 10 layer sample, the values for the thicker samples have smaller contributions from the dirty limit term and are thus mostly in the clean limit. The samples for high sheet resistance are dominated by the dirty limit contribution.

## 8 Pearl Length

In superconducting films where the thickness  $d$  is much smaller than the penetration depth  $\lambda_L$  ( $d \ll \lambda$ ), magnetic fields are weakly screened in the transverse direction and instead spread laterally over long distances. This lateral field penetration is characterized by the Pearl length, defined as

$$\Lambda = \frac{2\lambda^2}{d} \quad (27)$$

The Pearl lengths of all the devices in this work are estimated using Eq. 27, where the penetration depth of  $\text{NbSe}_2$  is 230 nm.

## 9 Determination of $\text{NbSe}_2$ Thickness and Layer Number

### 9.1 AFM characterization of hBN- $\text{NbSe}_2$ -hBN stack

Atomic force microscopy (AFM) is a high-resolution imaging technique used in this work to characterize the surface topography and height of hBN- $\text{NbSe}_2$ -hBN stacks. The thickness of hBN encapsulated  $\text{NbSe}_2$  is determined by tapping-mode AFM, illustrated in Fig. S8. The AFM measurement tends to overestimate the actual thickness of  $\text{NbSe}_2$  due to the presence of the top hBN encapsulation. In this work, the effective  $\text{NbSe}_2$  thickness is slightly smaller, as confirmed by the shear mode in the low-frequency Raman spectrum.

### 9.2 Raman Spectroscopy of thin $\text{NbSe}_2$ films

The number of layers in our samples was determined by the shear mode frequency of Raman spectroscopy [86, 87]. The Raman data were collected using a Horiba LabRAM Evolution system in the XY channel at room temperature. A 50x objective (Mitutoyo MY50X-825) was employed to direct and collect light in the backscattering geometry with a 532 nm wavelength. Data were captured using a liquid nitrogen-cooled CCD,

maintained at -133°C. The incident laser power on the sample was estimated to be below 4 mW. Figure S7b shows that the low-frequency mode observed in the Raman spectra corresponds to interlayer shear modes. In all spectra, shear modes are analyzed using Lorentzian peak fitting after subtracting the background. The shear mode peak in Raman spectra originates from interlayer shearing and is absent in the monolayer sample. The frequency of the shear modes ( $\omega_s$ ) decreases with decreasing layer number ( $N$ ), reflecting a reduced effective interlayer spring constant. The relationship can be described as  $\omega_s = \omega_{s,\text{Bulk}} \cos(\frac{\pi}{2N})$  with a bulk shear mode frequency  $\omega_{s,\text{Bulk}} = 29.39 \text{ cm}^{-1}$  [87, 88]. The AFM-measured thicknesses of the NbSe<sub>2</sub> flakes are consistent with the layer numbers determined from the shear mode frequency (1 layer = 1 nm) for all samples except for the thinnest device D1 (see main text table). For D1, the AFM measurement indicates a thickness of 2 nm, while Raman spectroscopy only shows a weak feature at the frequency 19.04 cm<sup>-1</sup> rather than a well-defined Lorentzian peak (Fig S7b). This corresponds to a layer number less than 2, with a fitted value of  $N = 1.5$  (Fig. S7a). We use this Raman-derived value (1.5 nm) in the analysis presented in Fig. 4a.

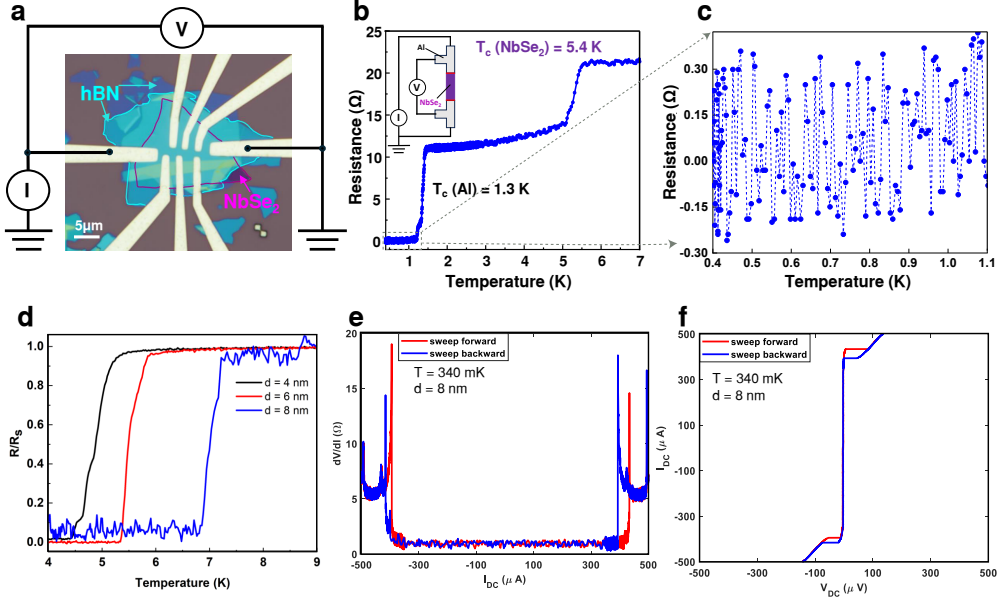


Figure S1: **Al and  $\text{NbSe}_2$  interface characterization and DC characteristics of  $\text{NbSe}_2$ .** **a**, Optical micrograph of a pseudo-4-probe DC device where hBN flakes fully encapsulate  $\text{NbSe}_2$  flake, the current is applied between two terminals, and voltage is measured across those two terminals without taking into account the line resistance of the measurement setup. **b**, Resistance(T) for Al- $\text{NbSe}_2$ -Al device showing the superconducting transition of  $\text{NbSe}_2$  ( $d = 6$  nm) at 5.4 K and the superconducting transition of Al at 1.3 K. Inset represents the 4-pt measurement setup for measuring the contact resistances of the Al/ $\text{NbSe}_2$  interfaces. **c**, Total Resistance of the device below Al transition, which has dropped to zero within the noise floor of the measurement. **d**, Temperature dependence of the resistance for devices with  $\text{NbSe}_2$  thicknesses of 4 nm, 6 nm, and 8 nm. To extract the  $T_c$ , we use the mean-field definition of  $T_c$ , which corresponds to half of the normal state resistance. **e**, Differential resistance ( $dV/dI$ ) measurement for the  $d = 8$  nm thick  $\text{NbSe}_2$  of 4-point DC measurement. The plot shows the critical current  $400 \mu\text{A}$  for that device. **f**, Current-voltage (I-V) relation on the same device.

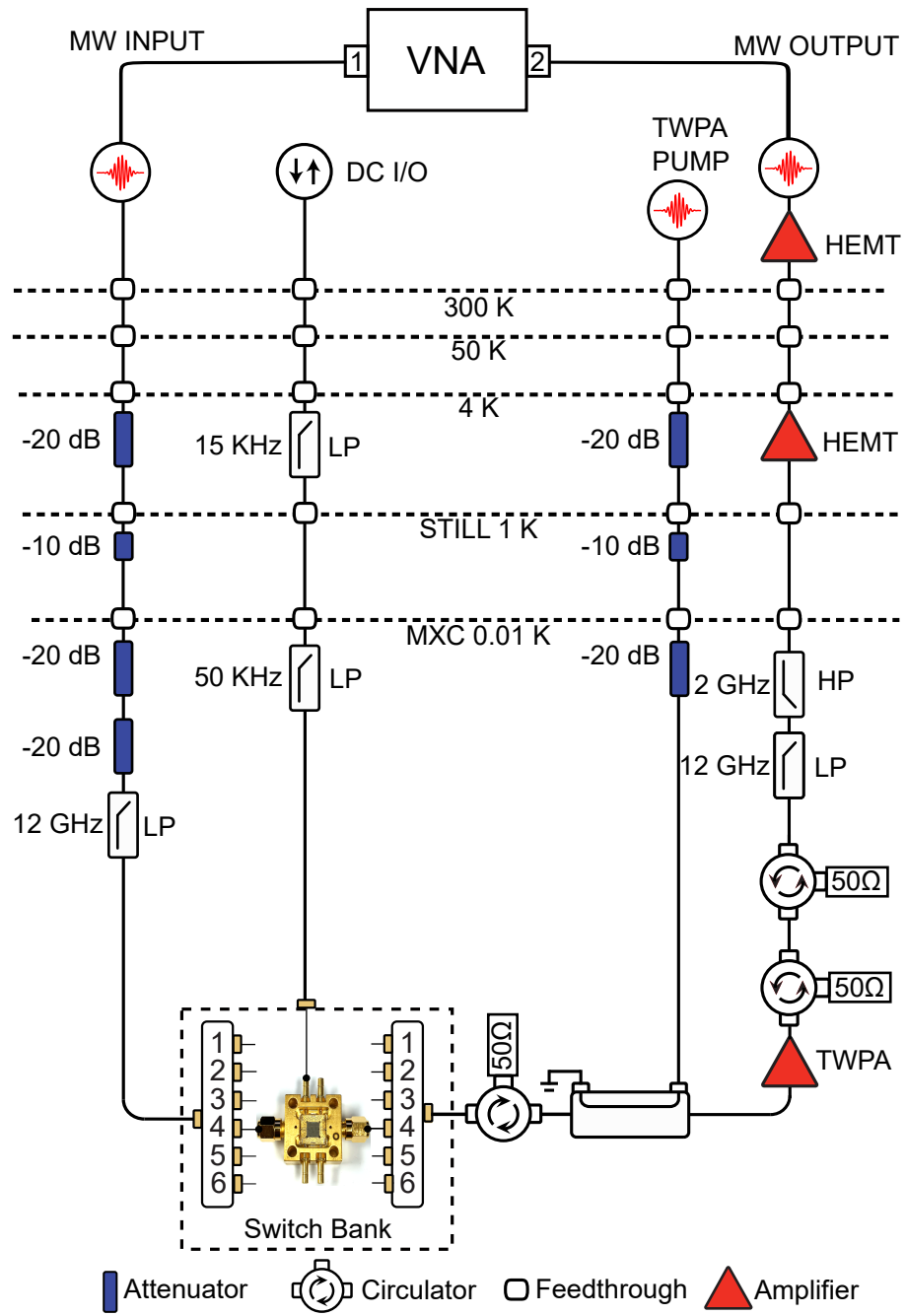


Figure S2: **Measurement setup.** Wiring diagram of the microwave and DC setup to the device.

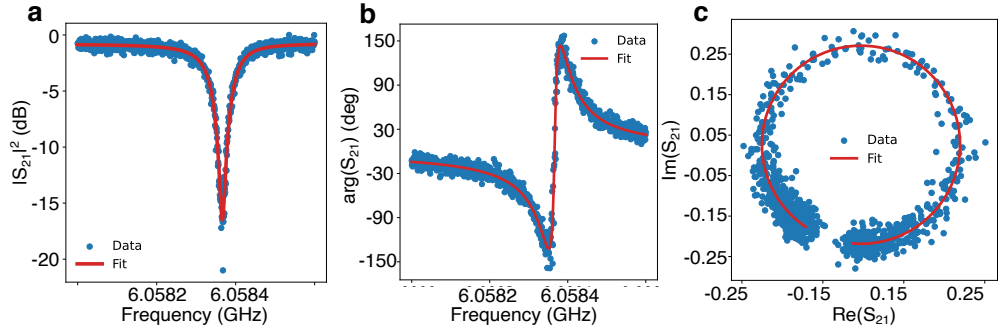


Figure S3: **Raw data (blue) and Lorentzian fit (red) of Al ‘spectator’  $\lambda/4$ -resonator.** **a-b** Magnitude and phase response of  $S_{21}$  signal as a function of frequency at the single photon limit. The equation 3 function is used to fit the complex response. **c**, The imaginary part of  $S_{21}$  is plotted versus its real part, where the circle diameter corresponds to  $Q_L/Q_c = \frac{Q_i/Q_c}{(Q_i/Q_c)+1}$ , which determines the contributions of coupling and internal losses of the resonator. The fitted resonance frequency is 6.0583 GHz, with an internal quality factor,  $Q_i$  is  $5.985 \times 10^6$ , and a coupling quality factor,  $Q_c$  is  $10^5$ .

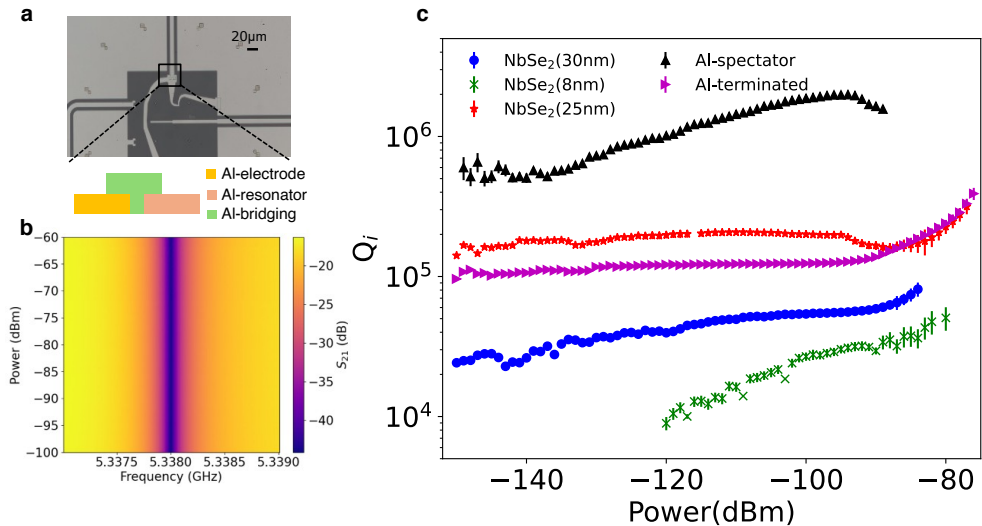


Figure S4: **Measurements of  $\lambda/4$  resonator.** **a**, Optical image of Al-terminated resonator of similar geometry used in Fig 3 (main text). Here, two different Al layers (one MBE grown (orange) and another e-beam evaporated (yellow)) are made contact through an aluminum bridging step (green). The bridging step is performed by doing in-situ ion-milling to remove the native oxide layer and evaporate another layer of aluminum. **b**, Magnitude response of Al-shunted resonator with varying the input microwave power from  $-100$  dBm to  $-60$  dBm. The resonant frequency has a very negligible change, showing a small contribution of kinetic inductance from aluminum. **c**, Comparison of quality factors across different types of  $\lambda/4$  resonators discussed in this work.

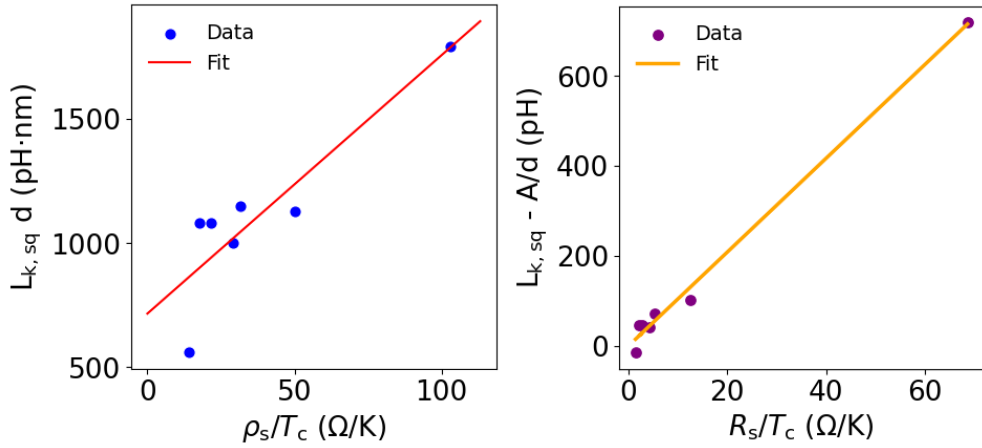


Figure S5: **a**, The linear relationship of  $L_{k,\text{sq}} \times d$  with  $\rho_s/T_c$  where the intercept of the y-axis sets the value of the fitting parameter  $A = \frac{m_{eff}}{n_0 e^2}$ . **b**,  $L_{k,\text{sq}} - \frac{A}{d}$  is plotted as a function of  $R_s/T_c$ , where the linear fit shows the dirty limit contribution for the thinner samples of  $\text{NbSe}_2$ .

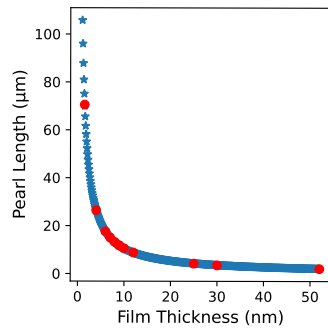


Figure S6: **Pearl length estimation (blue)** of  $\text{NbSe}_2$  of different thicknesses with consideration of  $\lambda_L = 230$  nm. The  $\text{NbSe}_2$  samples of this work are identified in red circles.

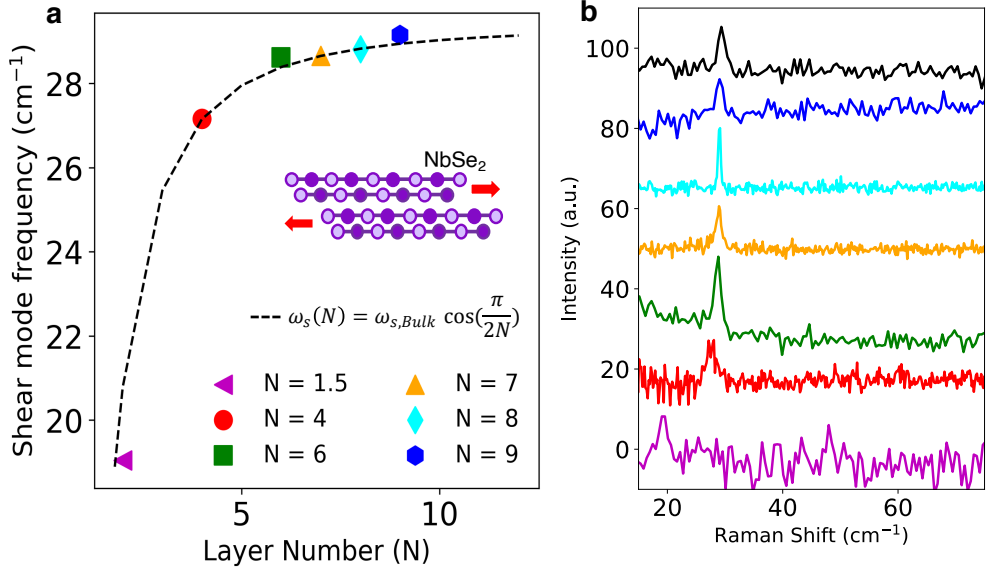


Figure S7: **Low-frequency Raman spectroscopy on different layers of  $\text{NbSe}_2$  samples at room temperature under vacuum for the perpendicular polarization configuration.** **a**, Plot of shear mode frequency versus layer numbers of  $\text{NbSe}_2$ . The dotted blue line shows the  $\omega_s = \omega_{s,Bulk} \cos(\frac{\pi}{2N})$  relation with  $\omega_{s,Bulk} = 29.39 \text{ cm}^{-1}$ . **b**, Low-frequency Raman spectra of  $\text{NbSe}_2$  with layer number  $N = 4 - 8$  and bulk  $\text{NbSe}_2$ . For clarity, the spectra are vertically displaced.

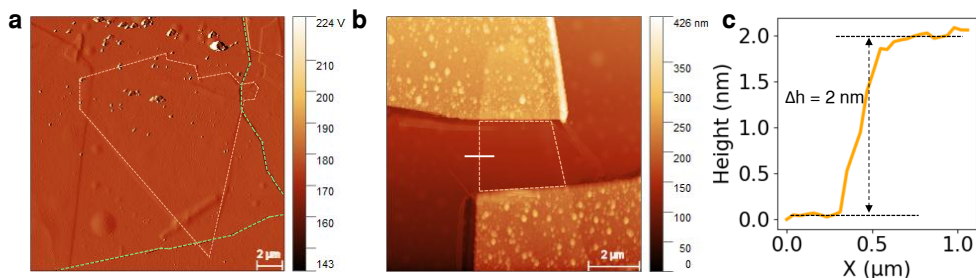


Figure S8: **AFM topographic image of hBN encapsulated  $\text{NbSe}_2$  devices.** **a**, Amplitude topography of the  $\text{NbSe}_2$  flake following the assembly of the hBN- $\text{NbSe}_2$ -hBN heterostructures (hBN-green and  $\text{NbSe}_2$ -orange). **b**, Height profile along the indicated path (white line) to determine the thickness of  $\text{NbSe}_2$ .